

Towards constraining cosmological parameters with SPT-3G observations of 25% of the sky

A. Vitrier ,¹ K. Fichman,^{2,3,4} L. Balkenhol ,¹ E. Camphuis ,¹ F. Guidi ,¹ A. R. Khalife ,¹

A. J. Anderson ,^{5,3,6} B. Ansarinejad,⁷ M. Archipley ,^{6,3} K. Benabed,¹ A. N. Bender ,^{4,3,6}

B. A. Benson ,^{5,3,6} F. Bianchini ,^{8,9,10} L. E. Bleem ,^{4,3,6} F. R. Bouchet ,¹ L. Bryant,¹¹

M. G. Campitiello,⁴ J. E. Carlstrom ,^{3,11,2,4,6} C. L. Chang,^{4,3,6} P. Chaubal,⁷ P. M. Chichura ,^{2,3}

A. Chokshi,⁶ T.-L. Chou ,^{6,3,12} A. Coerver ,¹³ T. M. Crawford ,^{6,3} C. Daley ,^{14,15} T. de Haan ,¹⁶

K. R. Dibert,^{6,3} M. A. Dobbs,^{17,18} M. Doohan,⁷ A. Doussot,¹ D. Dutcher ,¹⁹ W. Everett,²⁰ C. Feng,²¹

K. R. Ferguson ,^{22,23} N. C. Ferree ,^{24,8,9} A. Foster ,¹⁹ S. Galli,¹ A. E. Gambrel,³ R. W. Gardner,¹¹

F. Ge,^{24,8,9,25} N. Goeckner-Wald,^{9,8} R. Gualtieri ,^{4,26} S. Guns,¹³ N. W. Halverson,^{27,28} E. Hivon ,¹

G. P. Holder ,²¹ W. L. Holzapfel,¹³ J. C. Hood,³ A. Hryciuk,^{2,3} N. Huang ,¹³ F. Kéruzoré,⁴ L. Knox,²⁵

M. Korman,²⁹ K. Kornelje,^{6,3,4} C.-L. Kuo,^{8,9,10} K. Levy,⁷ Y. Li ,³ A. E. Lowitz ,³ C. Lu,²¹ G. P. Lynch ,²⁵

A. Maniyar,^{8,9,10} E. S. Martsen,^{6,3} F. Menanteau,^{15,30} M. Millea ,¹³ J. Montgomery,¹⁷ Y. Nakato,⁹ T. Natoli,³

G. I. Noble ,^{31,32} Y. Omori,^{6,3} A. Ouellette,²¹ Z. Pan ,^{4,3,2} P. Paschos,¹¹ K. A. Phadke ,^{15,30,33}

A. W. Pollak,⁶ K. Prabhu,²⁵ W. Quan,^{4,2,3} M. Rahimi,⁷ A. Rahlin ,^{6,3} C. L. Reichardt ,⁷ M. Rouble,¹⁷

J. E. Ruhl,²⁹ E. Schiappucci,⁷ A. C. Silva Oliveira ,^{24,8,9} A. Simpson,^{6,3} J. A. Sobrin ,^{5,3} A. A. Stark,³⁴

J. Stephen,¹¹ C. Tandoi,¹⁵ B. Thorne,²⁵ C. Trendafilova,³⁰ C. Umlpta ,²¹ J. D. Vieira ,^{15,21,30}

Y. Wan,^{15,30} N. Whitehorn ,²³ W. L. K. Wu ,^{24,8,10} M. R. Young,^{5,3} and J. A. Zebrowski,^{3,6,5}

(SPT-3G Collaboration)

¹*Sorbonne Université, CNRS, UMR 7095, Institut d’Astrophysique de Paris, 98 bis bd Arago, 75014 Paris, France*

²*Department of Physics, University of Chicago, 5640 South Ellis Avenue, Chicago, IL, 60637, USA*

³*Kavli Institute for Cosmological Physics, University of Chicago,*

5640 South Ellis Avenue, Chicago, IL, 60637, USA

⁴*High-Energy Physics Division, Argonne National Laboratory,*

9700 South Cass Avenue, Lemont, IL, 60439, USA

⁵*Fermi National Accelerator Laboratory, MS209, P.O. Box 500, Batavia, IL, 60510, USA*

⁶*Department of Astronomy and Astrophysics, University of Chicago,*

5640 South Ellis Avenue, Chicago, IL, 60637, USA

⁷*School of Physics, University of Melbourne, Parkville, VIC 3010, Australia*

⁸*Kavli Institute for Particle Astrophysics and Cosmology,*

Stanford University, 452 Lomita Mall, Stanford, CA, 94305, USA

⁹*Department of Physics, Stanford University, 382 Via Pueblo Mall, Stanford, CA, 94305, USA*

¹⁰*SLAC National Accelerator Laboratory, 2575 Sand Hill Road, Menlo Park, CA, 94025, USA*

¹¹*Enrico Fermi Institute, University of Chicago, 5640 South Ellis Avenue, Chicago, IL, 60637, USA*

¹²*National Taiwan University, No. 1, Sec. 4, Roosevelt Road, Taipei 106319, Taiwan*

¹³*Department of Physics, University of California, Berkeley, CA, 94720, USA*

¹⁴*Université Paris-Saclay, Université Paris Cité,*

CEA, CNRS, AIM, 91191, Gif-sur-Yvette, France

¹⁵*Department of Astronomy, University of Illinois Urbana-Champaign,*

1002 West Green Street, Urbana, IL, 61801, USA

¹⁶*High Energy Accelerator Research Organization (KEK), Tsukuba, Ibaraki 305-0801, Japan*

¹⁷*Department of Physics and McGill Space Institute, McGill University,*

3600 Rue University, Montreal, Quebec H3A 2T8, Canada

¹⁸*Canadian Institute for Advanced Research, CIFAR Program in*

Gravity and the Extreme Universe, Toronto, ON, M5G 1Z8, Canada

¹⁹*Joseph Henry Laboratories of Physics, Jadwin Hall,*

Princeton University, Princeton, NJ 08544, USA

²⁰*Department of Astrophysical and Planetary Sciences,*

University of Colorado, Boulder, CO, 80309, USA

²¹*Department of Physics, University of Illinois Urbana-Champaign,*

1110 West Green Street, Urbana, IL, 61801, USA

²²*Department of Physics and Astronomy, University of California, Los Angeles, CA, 90095, USA*

²³*Department of Physics and Astronomy, Michigan State University, East Lansing, MI 48824, USA*

²⁴*California Institute of Technology, 1200 East California Boulevard., Pasadena, CA, 91125, USA*

²⁵*Department of Physics & Astronomy, University of California, One Shields Avenue, Davis, CA 95616, USA*

²⁶*Department of Physics and Astronomy, Northwestern University, 633 Clark St, Evanston, IL, 60208, USA*

²⁷*CASA, Department of Astrophysical and Planetary Sciences,*

University of Colorado, Boulder, CO, 80309, USA

²⁸Department of Physics, University of Colorado, Boulder, CO, 80309, USA

²⁹Department of Physics, Case Western Reserve University, Cleveland, OH, 44106, USA

³⁰Center for AstroPhysical Surveys, National Center for Supercomputing Applications, Urbana, IL, 61801, USA

³¹Dunlap Institute for Astronomy & Astrophysics, University of Toronto,
50 St. George Street, Toronto, ON, M5S 3H4, Canada

³²David A. Dunlap Department of Astronomy & Astrophysics,
University of Toronto, 50 St. George Street, Toronto, ON, M5S 3H4, Canada

³³NSF-Simons AI Institute for the Sky (SkAI), 172 E. Chestnut St., Chicago, IL 60611, USA

³⁴Center for Astrophysics / Harvard & Smithsonian,
60 Garden Street, Cambridge, MA, 02138, USA

(Dated: November 3, 2025)

The South Pole Telescope (SPT), using its third-generation camera, SPT-3G, is conducting observations of the cosmic microwave background (CMB) in temperature and polarization across approximately $10\,000 \text{ deg}^2$ of the sky at 95, 150, and 220 GHz. This comprehensive dataset should yield stringent constraints on cosmological parameters. In this work, we explore its potential to address the Hubble tension by forecasting constraints from temperature, polarization, and CMB lensing on Early Dark Energy (EDE) and the variation in electron mass in spatially flat and curved universes. For this purpose, we investigate first whether analyzing the distinct SPT-3G observation fields independently, as opposed to as a single, unified region, results in a loss of information relevant to cosmological parameter estimation. We develop a realistic temperature and polarization likelihood pipeline capable of analyzing these fields in these two ways, and subsequently forecast constraints on cosmological parameters. Our findings indicate that any loss of constraining power from analyzing the fields separately is primarily concentrated at low multipoles ($\ell < 50$) and the overall impact on the relative uncertainty on standard ΛCDM parameters is minimal ($< 3\%$). Our forecasts suggest that SPT-3G data should improve by more than a factor of 300 and 3000 the Figure of Merit (FoM) of the EDE and the varying electron mass models, respectively, when combined with *Planck* data. The likelihood pipeline developed and used in this work is made publicly available online.^a

CONTENTS

I. Introduction	2	1. The <i>Polspice</i> procedure	16
II. SPT-3G and the Ext-10k survey footprint	3	2. The <i>apodizesigma</i> parameter and the <i>Wide</i> fields case	16
III. Methodology	5	B. Coadded covariance	17
A. Likelihood	5	C. Transfer functions	17
B. Forecasts	5	References	19
C. Covariance matrix	5		
D. Model	6		
E. Mock-data vector	7		
F. Cases considered	7		
G. Lensing likelihood	7		
H. Combination with <i>Planck</i>	8		
IV. Results	8		
A. Analysis strategy validation	8	I. INTRODUCTION	
B. Ext-10k forecasts	9		
1. ΛCDM	9	Over the last 30 years, observations of the cosmic	
2. Extended models	12	microwave background (CMB) have steadily driven	
V. Conclusions	14	advances in our understanding of the Universe. The	
VI. Acknowledgements	15	statistical properties of the CMB, as revealed by the	
A. <i>Polspice</i> <i>apodizesigma</i> value determination for	16	European Space Agency's <i>Planck</i> satellite and the latest	
the <i>Wide</i> fields		measurements from the South Pole Telescope (SPT) [1, 2]	

^a https://github.com/SouthPoleTelescope/spt_candl_forecasts

Over the last 30 years, observations of the cosmic microwave background (CMB) have steadily driven advances in our understanding of the Universe. The statistical properties of the CMB, as revealed by the European Space Agency's *Planck* satellite and the latest measurements from the South Pole Telescope (SPT) [1, 2] and the Atacama Cosmology Telescope (ACT) [3], are all consistent with the standard Λ Cold Dark Matter (ΛCDM) cosmological model, and constrain most of its parameters at better than the percent level [2–4]. Despite these successes, old and new questions remain unresolved. These include the nature of dark matter and dark energy, as well as the origin of primordial perturbations. More recently, the precision of the current data is leading to tensions in some parameter values. The underlying causes of the Hubble tension [5] and the emerging tension between Baryon Acoustic Oscillations (BAO) and CMB data [6, 7] are unclear regarding the extent to which they may be due to new physics or unknown systematic errors.

Ongoing and planned CMB experiments aim to address these questions by unveiling new information in the CMB temperature anisotropies at small angular scales and in the polarization of the CMB at all angular scales. These include the Simons Observatory [8] and the ongoing set of surveys with the third generation camera on the SPT, SPT-3G [9–11]. SPT-3G deep observations will also enable delensing of degree-scale B-mode polarization maps from the BICEP/Keck family of telescopes, which will sharpen the search for primordial gravitational waves from inflation [12].

In total, SPT-3G has surveyed 25% of the sky in frequency bands centered at 95, 150, and 220 GHz, with coadded sensitivity between three and 17 times higher than *Planck*¹ and with five times better resolution. The SPT-3G observations have been primarily divided into three surveys: the *Main* field, observed for five austral winter seasons; the *Summer* fields, observed for four austral summer seasons; and the *Wide* fields, observed for one entire year.

We define the combined SPT-3G surveys, covering a total of $10\,000 \text{ deg}^2$, as Ext-10k. The Ext-10k SPT-3G survey is anticipated to yield stringent constraints on cosmological parameters. Notably, [11] forecasted that Ext-10k observations could improve constraints on certain cosmological parameters within both ΛCDM and extended models up to a factor of two compared to *Planck* results and up to a factor of three when combined with *Planck* data. These forecasts, however, assumed the *Main*, *Summer*, and *Wide* fields to be five aggregated sky patches, one for the *Main* field, three for the *Summer* fields, and one for the *Wide* fields. However, in reality the *Wide* fields consist of nine distinct regions. Thus, in total, the Ext-10k survey is composed of 13 individual regions which exhibit unique observational characteristics, including variations in observation elevation, atmospheric contamination, Galactic foreground contamination, and noise properties. To accurately account for these specificities, the most straightforward approach is to treat all fields independently.

In this paper, we investigate whether this independent analysis approach allows us to fully capture the cosmological information encoded in the observed sky. Specifically, we address the question of whether analyzing the fields separately diminishes their constraining power by neglecting the correlations between pixels across different fields, which also impacts access to larger angular scale modes. To answer this question, we compare the constraints on ΛCDM cosmological parameters obtained from two distinct analysis approaches: one treating the entire survey as a single, contiguous field, and another treating it as 13 separate fields. To isolate the impact of the neglected correlations, we perform

this comparison assuming identical noise levels across all fields in both analysis scenarios, specifically adopting the noise properties characteristic of the *Wide* fields.

We perform this investigation for the CMB power spectra in temperature (TT), polarization (EE), and the cross-correlation between the two (TE). We find that the impact on ΛCDM cosmological parameter constraints is less than 3%. We thus adopt the separate-field approach to build mock likelihoods for the full-depth *Main*, *Summer*, and *Wide* fields using their own proper noise, and forecast cosmological parameters. We confirm the findings of [11] in ΛCDM and extend the forecasting work on models proposed to solve the Hubble tension as in [13]. For this part, we also develop a lensing reconstruction mock likelihood.

The paper is organized as follows: in Section II we describe the Ext-10k survey. Section III then details how we build the likelihoods and Fisher Matrices to forecast constraints. We present our results in Section IV and we summarize our conclusions in Section V.

II. SPT-3G AND THE EXT-10K SURVEY FOOTPRINT

The SPT is a 10-meter diameter telescope [14] located at the Amundsen-Scott South Pole station. The telescope has arcminute angular resolution and is currently equipped with its third-generation survey camera, SPT-3G. The SPT-3G focal plane consists of approximately 16 000 polarization-sensitive detectors that observe in three frequency bands centered at 95, 150, and 220 GHz [9, 10].

SPT-3G has been used to survey approximately $10\,000 \text{ deg}^2$ of the Southern sky, providing a powerful dataset for cosmology. The survey is partitioned into different observational fields, each optimized to fulfill different scientific objectives and operational constraints. The fields are defined as follows:

Main: During the Austral winter, spanning roughly eight months annually, SPT-3G has primarily been used to observe a 1500 deg^2 *Main* field. This field has the lowest Galactic foreground contamination. From data obtained between 2019 and 2023, the field has been measured to a coadded sensitivity of approximately $1.9 \mu\text{K-arcmin}$, the deepest of any of the SPT-3G fields. The *Main* field will be observed for at least two more winter seasons, further improving the coadded sensitivity to $< 1.6 \mu\text{K-arcmin}$. The deep integration within this region enables a precise measurement of polarization E-modes. This measurement and the reconstructed lensing potential will be used to delens the data of the BICEP/Keck experiment [2] and to set tight constraints on the tensor-to-scalar ratio [12, 16].

Summer: During the Austral summer, starting in early December through the middle of March, the Sun contaminates the *Main* field. During this period between 2019 and 2023, SPT-3G observed three distinct *Summer*

¹ The *Planck* 2018 data has temperature white noise levels of 77, 33, and $47 \mu\text{K-arcmin}$ at 100, 143, and 217 GHz, corresponding to a coadded sensitivity of $27.6 \mu\text{K-arcmin}$.

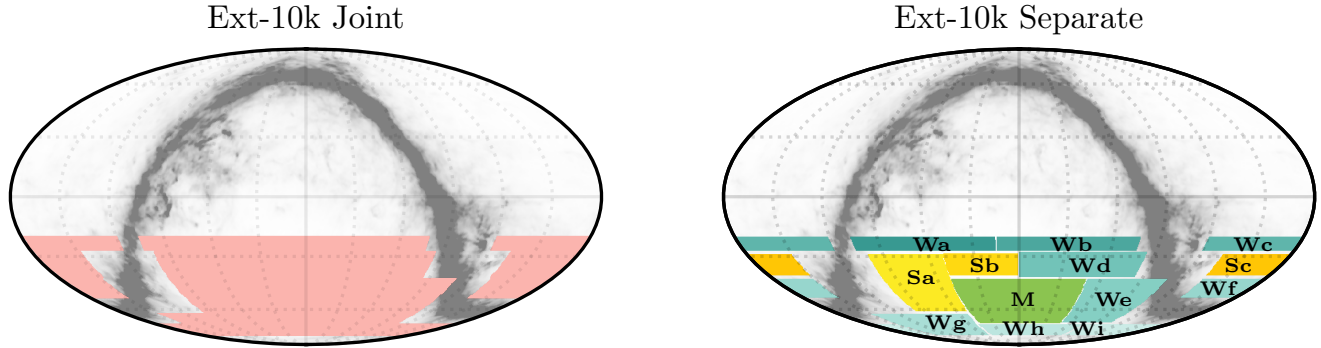


FIG. 1. Observed sky area with joint (left) and separated (right) masks used to perform either a global or a separate analysis of the Ext-10k survey, which spans declinations from -20° to -80° . The *Main* field (in green) is denoted by M, the three *Summer* fields (in yellow) are Sa, Sb, and Sc, and the nine *Wide* fields (in blue) are named from Wa to Wi. The masks are shown in equatorial coordinates and are superposed on the **Commander** dust map produced in the component separation of the *Planck* analysis [15]. The dashed lines are 30° intervals between meridians and between parallels. The vertical and horizontal solid lines correspond to $\text{RA} = 0$ and $\text{dec} = 0$, respectively.

	Main	Summer			Wide								
		a	b	c	a	b	c	d	e	f	g	h	i
$f_{\text{sky}} [\%]$	4.04	2.92	1.31	1.94	1.28	1.28	1.67	2.04	2.03	1.22	1.12	0.65	0.65
Coadded sensitivity [$\mu\text{K-arcmin}$]	1.9	6.2	6.8	6.6						8.8			

TABLE I. Fraction of the total sky, f_{sky} , and coadded sensitivities of the 13 fields of the Ext-10k survey. The f_{sky} values are based on the masks used in the Ext10k_{sep} analysis. The *Main* field is the biggest field and covers 4% of the total sky, while the *Wide* h and i fields each cover only 0.65%. The *Summer* fields and the *Wide* fields cover 6% and 12% of the sky, respectively, after apodizing each field individually.

fields totaling approximately 2600 deg^2 to a coadded sensitivity of approximately $6 \mu\text{K-arcmin}$. Although less deep than the *Main* field, the expanded sky coverage reduces sample variance in CMB power spectra measurements on large angular scales, thereby improving overall cosmological parameter constraints.

Wide: Between 2023 and 2024, SPT-3G observed nine fields covering an additional 6000 deg^2 in what we call the *Wide* survey. This survey targets all sky regions accessible from the South Pole within instrumentally feasible elevations, ranging from approximately 20° to 80° , while avoiding the Galactic plane.² The *Wide* fields are the shallowest of the three surveys, measured to a coadded sensitivity of approximately $9 \mu\text{K-arcmin}$. However, the additional area helps to further reduce sample variance of the combined SPT-3G Ext-10k survey measurements. The nine *Wide* fields were defined and observed to minimize contamination from the Moon, Sun, and atmosphere, while still maintaining a high observing efficiency. At low elevations, the Moon passes through some observation fields. Field observations were

scheduled to avoid Moon contamination over the lunar cycle. Similarly, during the Austral summer when the Sun is above the horizon, only fields through which the Sun does not pass are observed. To minimize atmospheric contamination, low-elevation fields were observed during the Austral winter, while high-elevation fields were observed during the Austral summer.

The footprints of the *Main*, *Summer*, and *Wide* fields are shown in Figure 1. The masks used in this work are produced in HEALPix³ [17] at $N_{\text{side}} = 2048$.⁴ The binary masks are then apodized to reduce ringing in harmonic space for power spectrum estimation and to reduce correlations between modes. We apodize with the equivalent of a Gaussian taper of width $\sigma = 34 \text{ arcmin}$. The apodization algorithm is the same as the one described in Appendix A of [18]. Table I summarizes the f_{sky} values for the 13 different fields of the survey.

While the *Wide* fields observations are designed to avoid the Galactic plane, some highly emissive Galactic regions are still included in the survey and will be masked in the real analysis. In this work, we do not account for

² *Wide* e partially scans through the Galactic plane for simplicity of definition of survey boundaries.

³ <https://healpix.sourceforge.io>

⁴ See Section 4 of [17] for the definition of N_{side} .

the masking of these contaminated regions but we verify that applying the GAL080 mask produced by the *Planck* collaboration [18, 19], which removes the 20% of the full sky most contaminated by Galactic dust emission, only changes the *Wide* field coverage from 14.4% to 13.2% of the total sky.

In the following sections, we will consider two ways of analyzing the Ext-10k survey. In the first method, which we call $\text{Ext10k}_{\text{joint}}$, we consider the 13 fields as a single patch surrounded by a common apodized border and covering 23% of the sky. In the second one, which we call $\text{Ext10k}_{\text{sep}}$, we consider the 13 separate fields of the Ext-10k survey, each having apodized borders, and covering 22% of the sky. The small difference between sky fractions is due to the loss of sky area due to the apodization of the 13 separate fields in the $\text{Ext10k}_{\text{sep}}$ case compared to the single field in the $\text{Ext10k}_{\text{joint}}$ case. Figure 1 shows the two cases.

III. METHODOLOGY

A. Likelihood

The realistic likelihoods we build to forecast the constraints on cosmological parameters in different settings are implemented in the JAX-friendly [20] fully differentiable CMB power spectra likelihood framework `candl`⁵ [21], which allows us to automatically estimate Fisher Matrices when coupled to the differentiable emulator `CosmoPower` [22, 23]. We build the likelihood of the mock-data given a model following the SPT-3G 2018 [24] likelihood as implemented in `candl`. Our analysis being at high ℓ with a sufficient number of independent modes, we assume the power spectrum amplitudes are Gaussian distributed. The likelihood thus takes the form:

$$-\ln \mathcal{L}(\vec{D}|\vec{D}(\theta)) = \frac{1}{2} \left[\vec{D} - \vec{D}(\theta) \right]^T \Sigma^{-1} \left[\vec{D} - \vec{D}(\theta) \right] + \text{const} \quad (1)$$

where \vec{D} is the data vector, $\vec{D}(\theta)$ is the model with parameters θ , and Σ is the covariance matrix.

B. Forecasts

We derive constraints on parameters either using a Fisher Matrix formalism for the Ext-10k TT/TE/EE analysis strategy validation, or a full Markov Chain Monte Carlo (MCMC) for the Ext-10k Λ CDM and extended models forecasts. The use of MCMC is necessary to explore highly non-Gaussian posterior distributions, such as those of the extended models (see Figure 9 as an example). For the calculation of the theory CMB

power spectra, we either use the Boltzmann solvers `CLASS` [25] or `CAMB` [26] or the emulator `CosmoPower`. For our forecasts, we adopt the same nuisance parameters as assumed in [24] (see Table VIII from that work). Finally, we use a Gaussian prior on τ with 0.054 as the central value and 0.0074 as the standard deviation $\mathcal{N} \sim (0.054, 0.0074)$, based on the *Planck* 2018 results [4].

The Fisher matrix is calculated from a second-order Taylor expansion of the likelihood around the best-fit parameters and allows us to forecast cosmological parameter constraints without any data. It depends on the power spectrum covariance matrix and on the theoretical power spectra as follows:

$$\mathcal{F}_{\alpha\beta} = \sum_{b_1, b_2} \sum_{XY, WZ} \frac{\partial D_{b_1}^{XY}}{\partial \theta^\alpha} [\text{Cov}(D_{b_1}^{XY}, D_{b_2}^{WZ})]^{-1} \frac{\partial D_{b_2}^{WZ}}{\partial \theta^\beta} \quad (2)$$

where $\{XY, WZ\} \in \{\text{TT}, \text{TE}, \text{EE}\}$ and θ^α refers to the cosmological and nuisance parameters. Thanks to our differentiable pipeline built on `CosmoPower-JAX` [22, 23] and `candl`, we can get accurate derivatives quickly using JAX. This allows us to calculate Fisher Matrices avoiding numerical difficulties associated with the finite difference method.

C. Covariance matrix

We calculate a realistic TT/TE/EE covariance matrix including several real data effects, as in [2]. We use an analytical calculation using the code developed in [27] and using a Narrow Kernel Approximation (NKA) [28, 29] to speed up the computations. The computation correctly accounts for the mode coupling introduced by the apodized footprint masks. In particular, it includes the effect of debiasing the pseudo- C_ℓ s from the effect of the mask using `Polspice` [30, 31], as described in Section 5.4 of [27]. In this work, we do not include the effect of masking point sources in the covariance, under the assumption that the Ext-10k analysis will inpaint over bright sources, as was done in [2]. For the fiducial cosmological model, the theory power spectrum is calculated from the *Planck* 2018 best-fit.⁶ The foreground levels at each frequency are based on the AGORA simulations [32], which include different extragalactic components such as the thermal Sunyaev–Zel’dovich (tSZ) and kinematic Sunyaev–Zel’dovich (kSZ) effects, cosmic infrared background (CIB), and radio sources. Those simulations do not include Galactic dust.

The noise power spectra used to build the covariance matrix are the same as the ones used and described in [11] for the full SPT-3G survey observations taken between 2019 and 2024. Namely, the *Main* field noise curves

⁵ <https://github.com/Lbalkenhol/candl>

⁶ `base_plikHM_TTTEEE_lowL_lowE_lensing`

include the five winter seasons from 2019 to 2023, the *Summer* field noise curves include four austral seasons between 2019 and 2023, and the *Wide* field noise curves correspond to one year of observation between 2023 and 2024. These noise spectra are modeled according to Equation 1 of [11] and include instrumental and atmospheric noise. The *Main* and *Summer* fields noise spectra are obtained by fitting real noise data to the model. The *Wide* fields noise curves have the same parametrization as the *Summer* noise curves, since real noise power spectra for the *Wide* fields did not exist when this work started. First preliminary measurements of the distinct *Wide* fields temperature noise spectra derived later show good agreement with the modeled noise power spectra. On top of these noise spectra we add a transfer function and a pixel window function which mimic the effect on the power spectrum of the time-ordered data (TOD) filtering and the integration of signal (or noise) over the pixel area, respectively. We show in Figure 2 the expected temperature noise power spectra of the *Wide* fields, the *Main* field, and the *Summer c* field (see [11] for details). Since *Summer a* and *Summer b* have comparable white noise levels as *Summer c*, we only show *Summer c* noise curves for comparison purposes with the *Wide* and *Main* fields.

We account for the impact of deconvolving the beams, the pixel window function, and the transfer function (see Figure 3), the computation of which is detailed in Appendix C. In particular, we account for the anisotropic nature of our filtering along the scan direction by rescaling the diagonal of the covariance matrix, as also detailed in Appendix C. The diagonal rescaling estimation from simulations is detailed in Section IV F of [2] and in Hivon et al., in prep. This rescaling is denoted $H(\ell)$ and is set to be equal to the transfer function based on Hivon et al., in prep, where this approximation is shown to be accurate at the 10% level for the *Main* and *Summer* fields.

D. Model

Our model vector $\vec{D}(\theta)$ is described by a set of cosmological and nuisance (foreground) parameters. The six Λ CDM cosmological parameters are the current expansion rate of the Universe H_0 , the baryon density $\Omega_b h^2$, the cold dark matter density $\Omega_c h^2$, the optical depth to reionization τ , and the amplitude A_s and spectral index n_s of the primordial scalar power spectrum. In addition to the cosmological parameters that affect the CMB theory spectra, we model the foreground parameters as in [24].

We account for the Poisson-distributed unresolved radio galaxies and dusty star-forming galaxies through 12 amplitude parameters for the six different auto- and cross-frequency spectra in temperature $D_{3000,\mu \times \nu}^{\text{TT,Poisson}}$ and in polarization $D_{3000,\mu \times \nu}^{\text{EE,Poisson}}$, where $\{\mu, \nu\} \in \{95, 150, 220\}$. The Galactic dust is modeled in TT, TE,

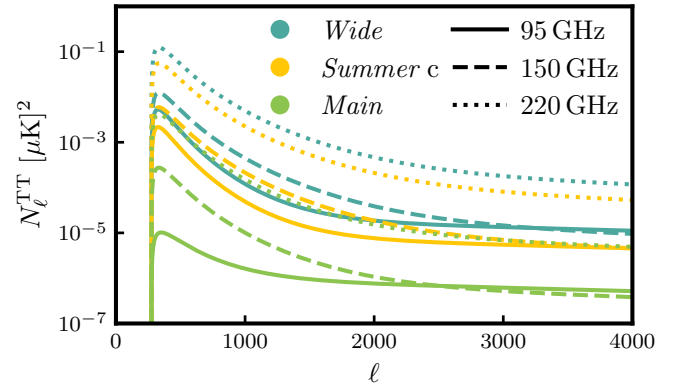


FIG. 2. Expected temperature noise power spectra for the *Wide*, *Summer c*, and *Main* fields for the three auto-frequencies 95 GHz \times 95 GHz, 150 GHz \times 150 GHz, and 220 GHz \times 220 GHz. They include the transfer function shown in Figure 3 and the pixel window function.

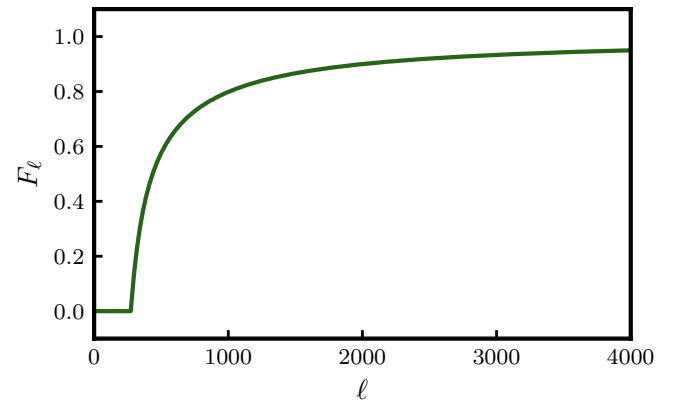


FIG. 3. Transfer function used in our TT/TE/EE analysis. This function describes the effect of the high-pass and low-pass filtering of the data on the power spectrum and the covariance matrix.

and EE by a modified black-body with an amplitude $A_{80}^{XY,\text{Dust}}$, a spectral index $\beta^{XY,\text{Dust}}$, and a power law index $\alpha^{XY,\text{Dust}}$, where $\{X, Y\} \in \{\text{T}, \text{E}\}$. We assume the dust contamination is constant across fields. The clustering term of the CIB is also modeled by a modified black-body spectrum with an amplitude $A_{3000}^{\text{CIB-cl}}$ and a spectral index $\beta_{3000}^{\text{CIB-cl}}$. We account for the tSZ and kSZ effects through two amplitude parameters A^{tSZ} and A^{kSZ} . The correlation between the tSZ and the CIB is modeled through the correlation parameter $\xi^{\text{tSZ} \times \text{CIB}}$. We also sample over super-sample lensing through a parameter κ in the same manner as [33]. Although the prior on this parameter depends on the field size [34] we decide to be conservative and use the *Main* field value, knowing that the prior for the Ext-10k real analysis will be tighter. We check that by fixing this parameter in our Λ CDM Ext-10k TT/TE/EE/ $\phi\phi$ forecasts, the only significantly

impacted parameter is H_0 , with the error bar reduced by 10%.

Our model does not account for instrumental systematics, such as the calibration and the beam. In the real analysis of one field, we sample over six calibration parameters for the three frequencies in temperature and polarization. In the real analysis of the Ext-10k survey, we will sample over 78 calibration parameters.

E. Mock-data vector

Our data vector is composed of binned simulated auto- and cross-frequency TT, TE, and EE power spectrum estimates, or band-powers. The bin width is chosen to be $\Delta\ell = 50$, as in previous SPT-3G TT/TE/EE analyses [2, 24], with $\ell_{\min} = 350$ and $\ell_{\max} = 4000$, also similar to previous analyses. In each bin there are eighteen total band-powers, comprising all possible combinations of T and E and the three frequency bands (95, 150, and 220 GHz). We treat TE and ET together for auto- and cross-frequencies. We assume that the data power spectra are always calculated from cross-correlating maps from different observation times to avoid noise bias. We build our simulated data as a smooth fiducial spectrum with `cand1`. The theory CMB is calculated from the *Planck* 2018 cosmological parameters (see Table 1 of [4]) using either Boltzmann solvers such as `CLASS` and `CAMB` or the `CosmoPower` emulator. For the latter, we use the SPT high accuracy models⁷ (see [24] for more details). The foregrounds at each frequency are modeled as in [24], where Table VIII summarizes the nuisance parameter central values used to produce our data vector.

We assume that in the real analysis the `Polspice` estimator is used to correct for the effect of the cut sky. Masking the sky suppresses the pseudo- C_ℓ power spectrum as described in Equation 14 of [30]. The `Polspice` procedure to correct for this effect is detailed in Appendix A 1 and the choices made within this procedure for the different fields are explained in Appendix A 2. Because of this correction, the `Polspice` spectra are biased and linked to the unbiased power spectra via the `Polspice` kernel (see also Section 6 of [27]). We take this into account in our data vector. The multiplication of the `Polspice` kernel and the binning matrix forms the window functions that compress the ℓ -by- ℓ spectrum into binned band-powers, $D_b = W_{b\ell}C_\ell$. Hence we obtain D_b from C_ℓ as follows:

$$D_b = Q_{b\ell'} K_{\ell'\ell} C_\ell \quad (3)$$

where K is the `Polspice` kernel and Q is the binning matrix which encapsulates the conversion from C_ℓ to D_ℓ , as detailed in Equation 28 of [2].

F. Cases considered

We build the likelihood for three different cases:

1. the Ext10k_{joint} case, where we treat the entire survey as one contiguous field with homogeneous noise levels equivalent to those of the *Wide* fields.
2. the Ext10k_{sep} case, where we treat the entire survey as 13 separate fields with homogeneous noise levels equivalent to those of the *Wide* fields.
3. the Ext10k_{sep}^{FD} case at full depth, where we treat the entire survey as 13 separate fields with the *Main*, *Summer* and *Wide* fields having their own distinct noise levels (see Table 1 of [11] for the detailed white noise levels of the different fields).

The comparison of the first two cases allows us to determine the impact of dividing the observed sky in 13 different regions, assuming the same noise levels in the two cases. The third case is the most realistic, with the proper noise curves for all the fields. We use this likelihood for the forecasts in Section IV. In the first case, only one covariance matrix is computed. In the second and third cases, we calculate 13 matrices. Note that in the three cases all the parameters which describe extragalactic foregrounds are assumed to be the same across all the fields. We also use one single set of parameters to describe the Galactic dust. However, in the third case we also test 13 different sets of parameters to capture the potentially different levels of contamination of each field.

G. Lensing likelihood

Forecasts are performed for TT/TE/EE, however we also build a mock lensing likelihood to compare our results with [11] and to forecast constraints on extended models in Section IV B. For this case, we build five separate likelihoods, one for the *Main* field, three for each *Summer* fields, and one for the whole *Wide* field. The CMB lensing analysis strategy will be investigated in a future work. The lensing data vector is composed of a normalized theory lensing potential spectrum $C_L^{\kappa\kappa} = [L(L+1)]^2 C_L^{\phi\phi} / 2\pi$ produced either by `CLASS` or `CAMB` from the same cosmological parameters as for the TT/TE/EE data vector. We then bin the lensing data vector with a bin size $\Delta L = 10$. We use the fiducial lensing potential spectrum $C_L^{\phi\phi}$ and the lensing reconstruction noise curves $N_L^{\phi\phi}$ used in [11] to produce the diagonal lensing analytic covariance matrices. The L range is $30 \leq L \leq 3500$ and we take into account the binning factor as follows:

$$\Sigma_{LL}^{\text{lensing}} = \frac{2}{(2L+1)f_{\text{sky}}\Delta L} (C_L^{\kappa\kappa} + N_L^{\kappa\kappa})^2. \quad (4)$$

⁷ https://github.com/alessiospuriomancini/cosmopower/tree/main/cosmopower/trained_models/SPT_high_accuracy

We do not include foregrounds in the lensing data vector or covariance. Our window function is the binning matrix.

H. Combination with *Planck*

In our forecasts, we also explore the combination of the Ext-10k survey with *Planck* for Λ CDM and extended models. In [11], it was shown that the full Ext-10k survey is expected to have higher constraining power than *Planck* at $\ell \gtrsim 1800$ for TT, $\ell \gtrsim 800$ for TE, $\ell \gtrsim 450$ for EE, and at all scales for $\phi\phi$.

In this work, we replace the real *Planck* data vector in the TT/TE/EE high- ℓ *Planck* likelihood `plik_rd12_HM_v22_TTTEEE.clik` by a theory power spectrum calculated with either CLASS or CAMB from the same cosmological parameters used for the SPT-3G TT/TE/EE and lensing data vectors. On top of this theory CMB, we also add a fiducial foreground and instrumental contribution assuming the *Planck* 2018 best-fit for the nuisance parameters.⁸ We perform the same ℓ -cuts as [11] in TT/TE/EE likelihoods to avoid double counting information, namely for the Ext-10k likelihoods we keep $\ell > 2000$ for TT, $\ell > 1000$ for TE, and $\ell > 750$ for EE. To apply these cuts, we use `clipy`⁹, a python implementation of the *Planck* data with JAX support. We do not use the *Planck* lensing likelihood and we keep all the scales in our SPT-3G Ext-10k lensing likelihoods. Moreover, we do not use *Planck* low ℓ EE likelihood but set the same τ prior $\mathcal{N} \sim (0.054, 0.0074)$ as in our forecasts without *Planck*. When exploring parameters, we assume that priors on the *Planck* nuisance parameters are the same as in the *Planck* 2018 analysis (see Table 16 of [35]).

IV. RESULTS

A. Analysis strategy validation

In this section, we compare the constraints from the Ext10k_{joint} and Ext10k_{sep} cases, using the same *Wide* field noise curves for both across the whole footprint. We include TT, TE, and EE band-powers between multipoles $\ell_{\min} = 350$ and $\ell_{\max} = 4000$. The ℓ_{\min} is chosen to cut out the scales suppressed by the filtering of the TOD, and it is similar to the choice adopted for the real data [2].

We first compare the band-power covariance matrices between the Ext10k_{joint} and Ext10k_{sep} cases. The ratio of the diagonal elements of the two matrices is shown in Figure 4. We detail the computation of the Ext10k_{sep}

⁸ `base_plikHM_TTTEEE_lowl_lowE_lensing`

⁹ <https://github.com/benabed/clipy>

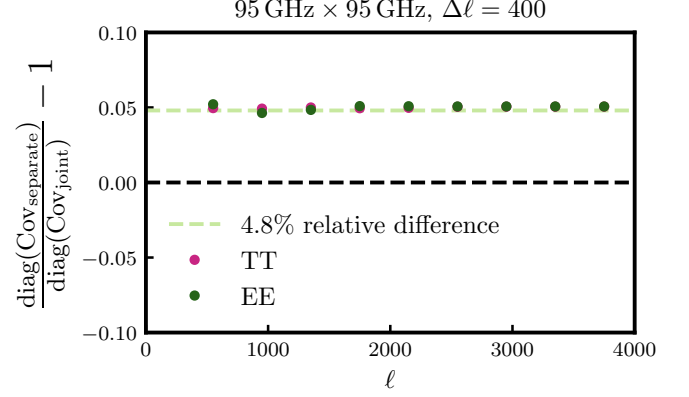


FIG. 4. Relative difference in the diagonal of the band-power covariance matrix between Ext-10k separate and joint analyses. We show TT and EE 95 GHz \times 95 GHz auto-frequency with a bin size $\Delta\ell = 400$ for $\ell_{\min} = 350$. The two diagonals differ by $\sim 5\%$ which corresponds to the 4.8% difference in sky fraction between the two cases due to the apodization of the individual masks in the Ext10k_{sep} analysis.

band-power covariance matrix in Appendix B. We show the ratio of the TT and EE 95 GHz \times 95 GHz diagonals after binning the covariance in $\Delta\ell = 400$ to decrease the bin-to-bin correlations so that the full constraining power is contained in the diagonal. The two cases differ by 5%. We obtain the same result for all the auto- and cross-frequency TT, TE, and EE diagonals. This difference corresponds to the decrease in sky fraction due to the additional apodized borders of the 13 fields in the Ext10k_{sep} case (the Ext10k_{joint} case has $f_{\text{sky}} = 0.2322$, while the Ext10k_{sep} case has $f_{\text{sky}} = 0.2215$, with a relative difference of 4.8%). Apart from this, we do not detect a significant difference between the two cases due to the loss of cross-field modes in the Ext10k_{sep} case.

We then compare the Fisher matrices calculated in the two cases for the Λ CDM model. This comparison is to verify how much the loss of f_{sky} affects constraints on parameters. In the Ext10k_{joint} analysis, we compute one Fisher matrix using the corresponding NKA covariance matrix, while in the Ext10k_{sep} analysis 13 Fisher matrices are obtained from the 13 NKA covariance matrices. We then sum the Fisher matrices together in order to obtain the final Fisher matrix of the separate analysis:

$$\mathcal{F}^{\text{sep}} = \sum_i \mathcal{F}^i. \quad (5)$$

The left diagram of Figure 5 shows the relative difference between the parameter covariance matrices obtained in the Ext10k_{sep} and Ext10k_{joint} cases. One can see that the differences in the diagonal, namely in the variance of each parameter, are small, of the order of $\sim 5\%$. These differences in parameter variance translate into differences of the order of $\sim 3\%$ in the resulting error bars, which is smaller than the numerical precision

in parameter estimation with an MCMC [36]. The largest relative difference is in the covariance between $\log(10^{10} A_s)$ and n_s , which is 50%. However, the absolute correlation value in the two cases is only -0.05 and -0.03 in the $\text{Ext10k}_{\text{sep}}$ and $\text{Ext10k}_{\text{joint}}$ cases, respectively. An increase of 50% of a small value has thus a negligible impact on the overall constraining power. We also show on the right hand side of Figure 5 the cosmological parameter correlation matrix in the $\text{Ext10k}_{\text{sep}}$ case.

We also calculate the Figure of Merit (FoM) for the two cases as follows:

$$\text{FoM} = \frac{1}{\sqrt{\det(\mathcal{F}^{-1})}} \quad (6)$$

where $\det(\mathcal{F}^{-1})$ is the determinant of the parameter covariance matrix. This FoM is the inverse of the volume space of the parameters, hence the higher this quantity, the tighter the parameter constraints. The six cosmological parameters's FoM in the joint case is $\text{FoM}_{\text{joint}} = 1.17 \times 10^{15}$ while for the separate case $\text{FoM}_{\text{sep}} = 1.06 \times 10^{15}$. The two FoM differ by 10%, the separate case having a lower FoM in comparison with the joint case as expected due to the difference in f_{sky} . This difference is negligible when comparing with *Planck* 2018 [4], the FoM ratio $\text{FoM}/\text{FoM}_{\text{Planck}}$ decreasing from 1.66 to 1.50 when going from the joint to the separate analysis.

We also test a case where we do not apply the transfer function shown in Figure 3 but instead apply a high-pass filter with a cutoff at $\ell = 50$ and set $\ell_{\text{min}} = 50$. $\ell = 50$ corresponds to an angular separation of approximately four degrees, which is close to the extent in declination of some fields such as the *Wide* a, b, or c fields. We find the same conclusion regarding the diagonal elements of the band-power covariance matrix, the parameter covariance matrices, and the FoM.

We conclude that the difference in constraining power between the $\text{Ext10k}_{\text{sep}}$ and $\text{Ext10k}_{\text{joint}}$ cases is negligible. Given the smallness of the effect both on band-power error bars and on the ΛCDM parameters, we do not explore the difference for extended models. Note that there is additional information in the $\text{Ext10k}_{\text{joint}}$ case if one uses ℓ_{min} smaller than 50. However, we do not consider this case, given the difficulty of measuring these modes with a ground-based experiment due to the low ℓ atmospheric noise. We thus establish that analyzing the fields separately as in the $\text{Ext10k}_{\text{sep}}^{\text{FD}}$ case is a viable analysis strategy without loss of information.

B. Ext-10k forecasts

Since the previous section demonstrated that the $\text{Ext10k}_{\text{sep}}^{\text{FD}}$ approach is a viable strategy, in this section we perform forecasts using the 13 likelihoods for TT, TE, and EE built for each of the fields, with the realistic noise levels of each field. For brevity, we will label $\text{Ext10k}_{\text{sep}}^{\text{FD}}$ as Ext-10k in the rest of this work. We include here the

simulated lensing likelihood described in Section III G and we derive realistic forecasts on cosmology from the full constraining power of the SPT-3G dataset by running MCMC using *Cobaya* [37]. We consider our chains to be converged when the Gelman-Rubin [38] statistic $R - 1$ reaches 0.02.

We first compare the results on ΛCDM with those of [11]. We then explore parameter constraints for three models that were selected in [13] which are the case of a varying electron mass [39], a varying electron mass in a spatially curved universe [40], and the case of Early Dark Energy (EDE) [41], the last two still being viable solutions to solve the Hubble tension.

1. ΛCDM

We first explore constraints with Ext-10k on the six cosmological parameters of the ΛCDM model. We sample over 33 parameters in total, including the six cosmological parameters and the 27 nuisance parameters defined in Section III D. Results are shown in Figure 6 and Table II. In Figure 6, we present three SPT-3G posterior distributions corresponding to Ext-10k TT/TE/EE, Ext-10k TT/EE/EE/φφ, and Ext-10k TT/TE/EE/φφ + *Planck* which can be compared to *Planck* PR3 constraints that include PR3 lensing. In Table II, we show the associated error bars at the 68% confidence level and the associated FoM relative to *Planck* PR3. Ext-10k TT/TE/EE constraints are obtained by combining our 13 TT/TE/EE likelihoods and using *CosmoPower* to calculate the theory CMB power spectra while the two other chains are computed using *CAMB* for the theory part. SPT-3G Ext-10k TT/TE/EE/φφ + *Planck* constraints are obtained by combining our 18 SPT-3G Ext-10k likelihoods with the *Planck* mock likelihood described in Section III H. For the latter we sample over the six cosmological parameters, the 27 SPT nuisance parameters, and the 21 *Planck* nuisance parameters, meaning that we sample over 54 parameters in total.

The SPT-3G Ext-10k TT/TE/EE uncertainties on the H_0 , $\Omega_b h^2$, A_s , and $\Omega_c h^2$ cosmological parameters are similar or lower compared to *Planck*. In particular, the Ext-10k TT/TE/EE $\Omega_b h^2$ error bar is 1.7 times smaller than the one from *Planck*. We also notice the importance of CMB lensing in tightening the parameter constraints, in particular for H_0 , $\Omega_c h^2$, and n_s , for which the constraints are improved by more than 30% when adding the lensing. SPT-3G Ext-10k TT/TE/EE/φφ will constrain ΛCDM cosmological parameters more tightly than *Planck* and twice better for $\Omega_b h^2$. Finally, adding *Planck* further contributes to tightening ΛCDM parameter constraints, improving all of them by more than a factor of 1.5 and by more than a factor of 2.2 for H_0 and $\Omega_b h^2$ in comparison with *Planck* alone.

We present additional constraints from SPT-3G Ext-10k TT/TE/EE/φφ alone or combined with *Planck* on the amplitude of matter density perturbations today σ_8 ,

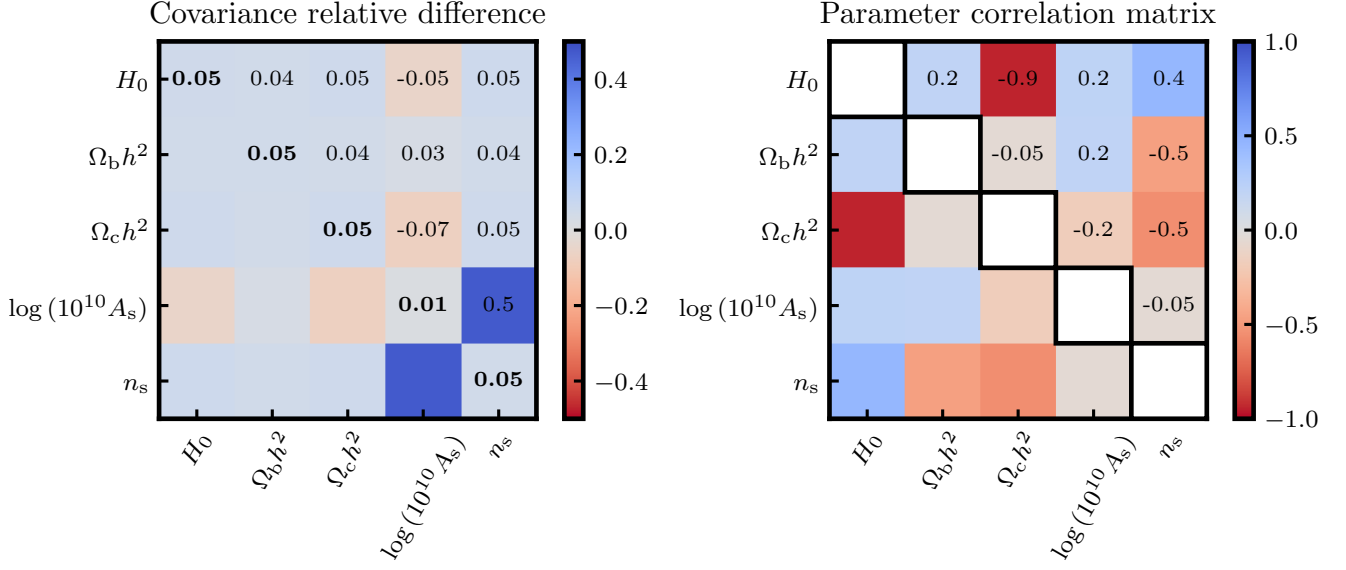


FIG. 5. *Left:* Relative difference in the parameter covariance matrix between Ext-10k separate and joint analyses. Analyzing the fields individually contributes to a $\sim 5\%$ increase of parameter variance. We do not show τ since it is prior driven. *Right:* Parameter correlation matrix for the Ext-10k separate analysis obtained from Fisher forecasting.

Parameter	Planck PR3	TT/TE/EE	TT/TE/EE/ $\phi\phi$	TT/TE/EE/ $\phi\phi$ + <i>Planck</i>
$H_0[\text{km s}^{-1} \text{ Mpc}^{-1}] [10^{-1}]$	5.4	5.1 (1.1)	3.1 (1.7)	2.5 (2.2)
$\Omega_b h^2 [10^{-5}]$	15	9.0 (1.7)	7.4 (2.0)	6.4 (2.3)
$\Omega_c h^2 [10^{-4}]$	12	13 (0.92)	7.3 (1.6)	6.3 (1.9)
$\log(10^{10} A_s) [10^{-3}]$	14	12 (1.2)	11 (1.3)	9.6 (1.5)
$n_s [10^{-3}]$	4.2	5.1 (0.82)	3.6 (1.2)	2.8 (1.5)
$\sigma_8 [10^{-3}]$	6.1		3.0 (2.0)	2.5 (2.4)
$\Omega_m [10^{-3}]$	7.4		4.4 (1.7)	3.7 (2.0)
$r_{\text{drag}} [\text{Mpc}] [10^{-1}]$	2.9		2.3 (1.3)	1.8 (1.6)
FoM/FoM _{Planck}	1	2.98	45.8	114

TABLE II. SPT-3G Ext-10k forecasts of Λ CDM cosmological parameter error bars at the 68% confidence level. Values in parentheses are the error bar ratios between *Planck* 2018 [4] and SPT-3G Ext-10k. They show by how much the error bars will be improved with SPT-3G Ext-10k in comparison with *Planck*. We do not show constraints on τ since they are prior driven. The last row presents the FoM relative to the *Planck* 2018 one. We forecast that SPT-3G Ext-10k TT/TE/EE/ $\phi\phi$ + *Planck* will constrain H_0 and $\Omega_b h^2$ twice as strongly as *Planck* alone.

the matter density Ω_m , and the sound horizon at the drag epoch r_{drag} . Posterior distributions for Ext-10k TT/TE/EE/ $\phi\phi$ and Ext-10k TT/TE/EE/ $\phi\phi$ + *Planck* are presented in Figure 7. We forecast that SPT-3G Ext-10k TT/TE/EE/ $\phi\phi$ alone will constrain σ_8 twice better than *Planck*, and that its combination with *Planck* will improve σ_8 and Ω_m constraints by more than a factor of two.

In computing these constraints, we use only one set of parameters to describe the Galactic dust. However, since the *Wide* and *Summer* fields have different locations

on the sky, some of them being much closer to the Galactic plane than others, we will be considering 13 different dust amplitudes in the real analysis. Hence, we perform a test in temperature and polarization with Fisher matrices to probe whether having 13 different sets of parameters to capture the potentially different levels of contamination of each field significantly degrades the cosmological parameter constraints. We forecast constraints on parameters with one single Galactic dust amplitude in temperature and with 13 different amplitudes, each of them having the same prior as the

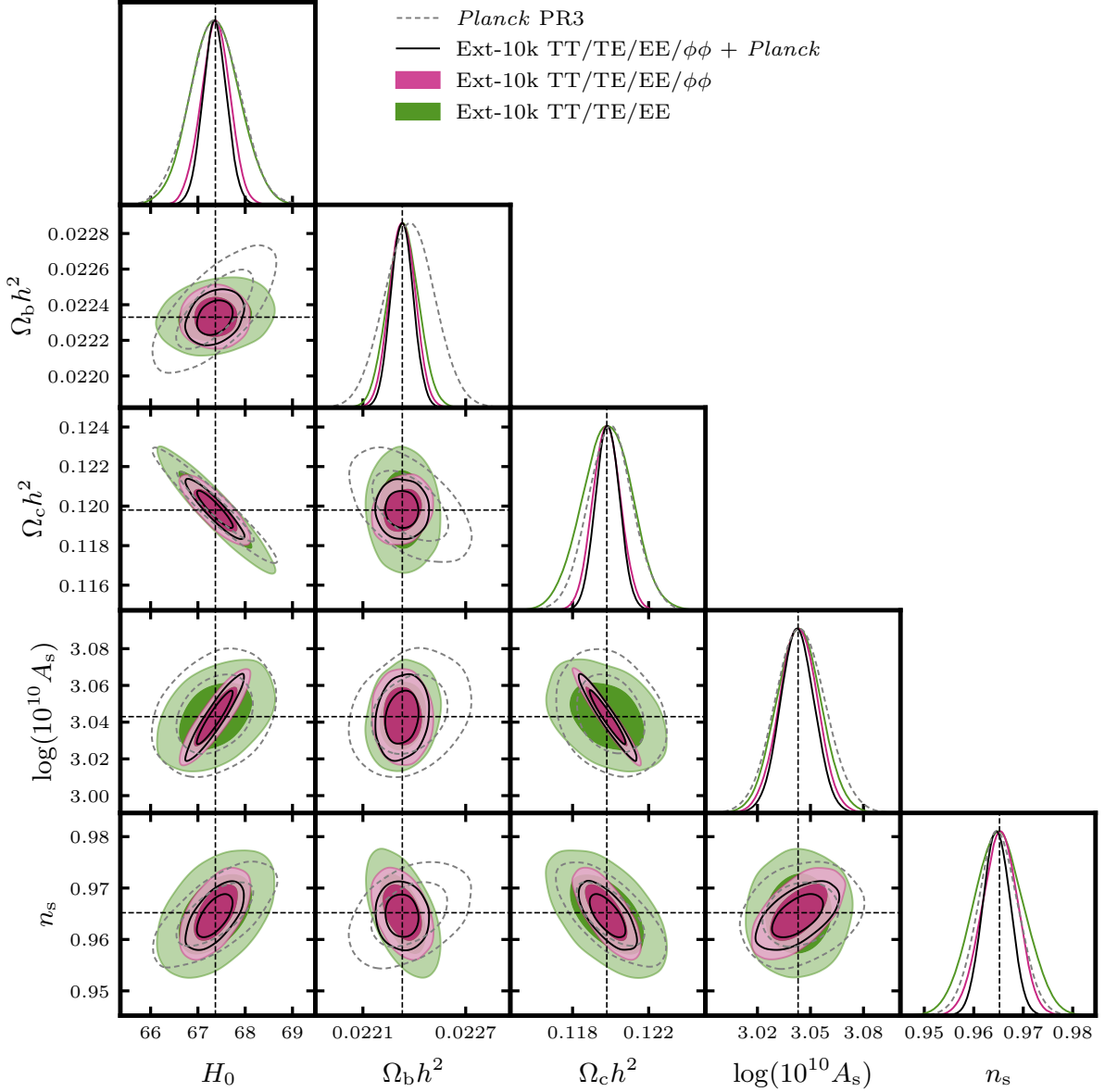


FIG. 6. SPT-3G Ext-10k forecasts of Λ CDM cosmological parameters. Contours correspond to the 68% and 95% confidence levels. We compare our results with *Planck* PR3 TT/TE/EE/φφ in gray dashed lines. The green contours show the posterior distributions of the parameters from temperature and polarization combining the 13 SPT-3G TT/TE/EE likelihoods. The pink contours are obtained by adding the five SPT-3G lensing likelihoods. The black line shows the combination of the 18 SPT-3G likelihoods with our mock *Planck* likelihood. The black dashed lines indicate the fiducial values used to produce our simulated band-powers. SPT-3G Ext-10k TT/TE/EE/φφ will constrain Λ CDM cosmological parameters more tightly than *Planck* and twice better for $\Omega_b h^2$.

one for the single amplitude $A_{80}^{\text{TT,Dust}}$, which is $\mathcal{N} \sim (1.88, 0.48)$ from [24]. The relative differences between the parameter covariance matrices computed in the two cases are of the order of $\sim 0.002\%$ in the diagonal. Increasing the standard deviation of the prior for the 13 amplitudes to 100 or 1000 does not affect the result. This small difference indicates that our results are robust to dust modeling.

Next, we check for the consistency of our results and

the ones of a previous work presented in [11]. The latter did not sample over nuisance parameters hence we also fix them to do this comparison. Fixing the nuisance parameters instead of varying them only changes the error bars of H_0 and $\Omega_b h^2$ by a small amount, with $\sigma(H_0)$ changing from 0.31 to $0.27 \text{ km s}^{-1} \text{ Mpc}^{-1}$ and $\sigma(\Omega_b h^2)$ changing from 7.4×10^{-5} to 7.2×10^{-5} . We find that our results are consistent across parameters to within 5%, which could be explained by some analysis differences.

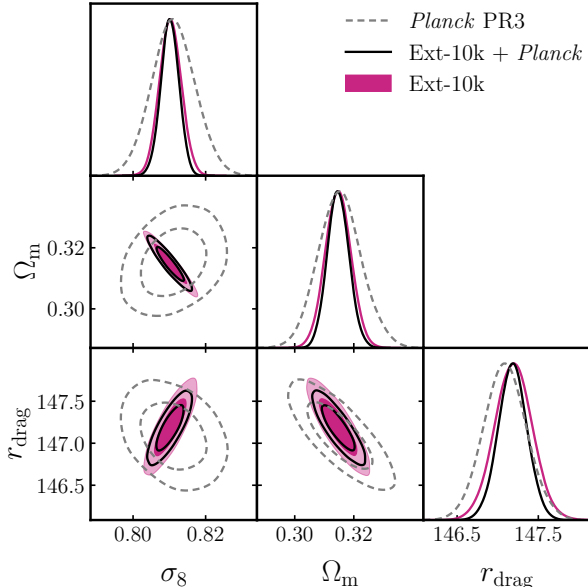


FIG. 7. SPT-3G Ext-10k forecasts of Λ CDM cosmological parameters σ_8 , Ω_m , and r_{drag} . Contours correspond to the 68% and 95% confidence levels. We compare our results with *Planck* PR3 TT/TE/EE/ $\phi\phi$ in gray dashed lines. The pink contours show the parameter posterior distribution from temperature, polarization, and lensing combining the 13 SPT-3G TT/TE/EE and five SPT-3G $\phi\phi$ likelihoods. The black line shows the combination of the SPT-3G Ext-10k TT/TE/EE/ $\phi\phi$ with our mock *Planck* likelihood.

For instance, a difference in the error bars is expected due to the different ways of computing the covariance matrix. In this work we use realistic analytical covariance matrices, while the forecasts shown in [11] are obtained with the MUSE method [42], a forward simulation based approach. According to [11], the two approaches should be consistent at the 10% level. Moreover, the τ prior used in [11] ($\mathcal{N} \sim (0.0544, 0.007)$) is 5% tighter than ours and the way the lensing is implemented in our analysis is also different since we build separate lensing mock likelihoods, while they build joint TT/TE/EE/ $\phi\phi$ band-power covariance matrices. We thus conclude that these small differences can account for the 5% discrepancies in the two works. Finally, when combining our SPT-3G Ext-10k likelihoods with the *Planck* mock likelihood described in Section III H to obtain final constraints on Λ CDM we find that our results are consistent at the 15% level with those of [11]. Since the two works use different ways of combining with *Planck* and marginalizing over the nuisance parameters, we consider a 15% difference to be reasonable. In particular, in this work we sample over the SPT nuisance parameters, and we use a τ prior instead of the *Planck* low ℓ EE likelihood. We conclude that our forecasts are compatible with those from [11] and consolidate them with a more realistic patch-based analysis with a foreground marginalization.

We also check that, with our forecasting pipeline, we

recover consistent Λ CDM constraints with the *Main* field real analysis of two years of observation in 2019 and 2020 [2]. For this purpose, we use the appropriate noise power spectra, which include two winter seasons from 2019 to 2020, and build a new NKA covariance matrix (see Section III C for further details). We perform our forecasts in temperature and polarization, and we obtain constraints on Λ CDM cosmological parameters that are between 15% and 25% tighter than [2]. A second test with the addition of the marginalization over the temperature and polarization calibration parameters only increases the cosmological parameter constraints by 2%, 5%, and 7% for H_0 , $\Omega_c h^2$, and $\log(10^{10} A_s)$, respectively, which does not fully explain the difference. This difference in the error bars is expected due to additional effects taken into account in the real analysis. For instance, the polarized beams model, described in Appendix B2 of [2], significantly degrades all parameter constraints, such as the n_s error bar which is widened by 20%. The contribution of gravitational lensing to the covariance matrix also increases the cosmological parameter error bars by 10%. We do not include the polarized beams model in this work since it was introduced in the real analysis after we started our forecasts. Moreover, a direct measurement of the polarized beams in the coming years should allow for the recovery of these tighter constraints.

We notice a small shift in our Ext-10k TT/TE/EE/ $\phi\phi$ + *Planck* posterior distribution for n_s and H_0 mean values compared to the fiducial values. This small shift is due to the fact that for two of the *Planck* nuisance parameters, A^{KSZ} and $\xi^{\text{tSZ} \times \text{CIB}}$, the posterior distributions are cut by the lower boundary of the uniform prior, which forces these amplitudes to be positive. The posterior distribution is thus sampled in an asymmetric way with respect to the peak of the distribution. This introduces a bias in the final distribution of other nuisance and cosmological parameters which are correlated with them. However, the shift is small and should not affect the computation of the error bars on cosmological parameters, which are the quantities of interest in this work.

Our constraints are obtained with a τ prior of $\mathcal{N} \sim (0.054, 0.0074)$, motivated by *Planck* 2018 results [4]. Removing this prior widens the constraints on τ , with $\sigma(\tau)$ changing from 0.0066 to 0.015 for Ext-10k TT/TE/EE/ $\phi\phi$, and from 0.0059 to 0.0097 for Ext-10k TT/TE/EE/ $\phi\phi$ + *Planck*. This shows that SPT-3G alone will not provide tight constraints on τ due to the inherent difficulty of measuring large scales with ground based experiments, these scales being crucial in polarization to constrain this parameter.

2. Extended models

In this section, we use our realistic SPT-3G Ext-10k TT/TE/EE and $\phi\phi$ mock likelihoods to explore different

extended models: two models with a varying electron mass and a model of EDE. SPT-3G has the potential to provide crucial insights into these models due to its precise measurement of small scales in polarization, particularly its measurement of the damping tail. The variation of the electron mass impacts recombination and its duration, which directly affects the damping scale, while Early Dark Energy impacts the expansion rate before recombination, thus affecting the recombination length. We use the same assumptions and details described in [13, 43]. Table III shows constraints on parameters for SPT-3G Ext-10k TT/TE/EE/ $\phi\phi$, SPT-3G Ext-10k TT/TE/EE/ $\phi\phi$ + *Planck*, and for *Planck* alone.

Note that we are including lensing information to high L 's and not including non-linear corrections for extended models, which could widen cosmological parameter error bars [44]. Figure 1 of [44] shows a small difference in Λ CDM cosmological parameter constraints when including or excluding non-linear corrections with lensing data. Error bars shrink slightly when non-linear corrections are enabled. We disable the non-linear corrections for extended models since the currently available codes such as **HALOFIT** [45] and **HMCODE** [46] do not include the corrections due to these models.

Varying electron mass. We test the varying electron mass model either in a spatially flat universe (m_e), where the curvature density parameter Ω_K is fixed to zero, or in a spatially curved space ($m_e + \Omega_K$), where it is allowed to freely vary. In the first case, we sample over seven cosmological parameters: the six common Λ CDM parameters, and the ratio of the early electron mass and the late electron mass $m_{e,\text{early}}/m_{e,\text{late}}$. In the second case, we sample over eight cosmological parameters by adding the curvature of the universe Ω_K . We use the model in which the mass of the electron transitions from a value $m_{e,\text{early}}$ to $m_{e,\text{late}}$ at redshift $z = 50$, with $m_{e,\text{late}}$ corresponding to the mass of the electron measured in laboratories. We use **CLASS** to compute the theoretical CMB power spectra of these two first models.

We show the results for SPT-3G Ext-10k TT/TE/EE/ $\phi\phi$ alone and combined with our *Planck* mock likelihood in Figure 8 and Figure 9 for m_e and $m_e + \Omega_K$, respectively. Similarly to the previous section on Λ CDM results, we observe a slight difference between the mean value of the parameters obtained from Ext-10k TT/TE/EE/ $\phi\phi$ alone and in combination with *Planck*, for the same reasons explained there.

Our forecasted SPT-3G Ext-10k constraints on H_0 and $m_{e,\text{early}}/m_{e,\text{late}}$ are a factor of three tighter than those from *Planck* in the two cases. We also compute the cosmological parameter FoM of these two models following Equation 6. Namely, the FoM is computed for seven and eight parameters for m_e and $m_e + \Omega_K$, respectively. We compare the FoM obtained for Ext-10k TT/TE/EE/ $\phi\phi$ and Ext-10k TT/TE/EE/ $\phi\phi$ + *Planck* with the one for *Planck* only. In the case of a flat universe with variable electron mass we find

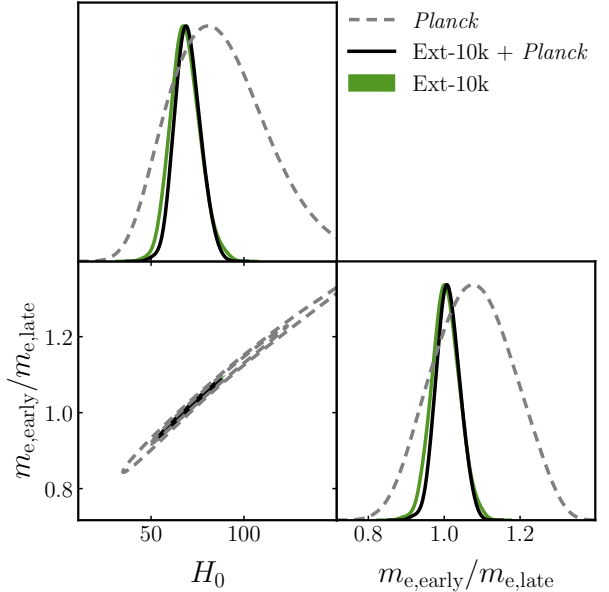


FIG. 8. SPT-3G Ext-10k TT/TE/EE/ $\phi\phi$ forecasts on the varying electron mass model in a flat universe. Contours correspond to the 68% and 95% confidence levels. In this plot, Ext-10k refers to Ext-10k TT/TE/EE/ $\phi\phi$ while *Planck* refers to our *Planck* mock likelihood.

that the Ext-10k TT/TE/EE/ $\phi\phi$ FoM is 1.21×10^3 times higher than the one from *Planck* and 3.15×10^3 times better when combining with *Planck*. In the case of varying electron mass in curved space the Ext-10k TT/TE/EE/ $\phi\phi$ FoM is 2.21×10^3 times higher than that from *Planck* alone and 6.36×10^3 times better when combining with *Planck*. We notice that combining with *Planck* does not significantly shrink the H_0 error bar in those two models in comparison with SPT-3G Ext-10k alone. However we can observe the benefit of combining with *Planck* on other parameter constraints, as shown in Table III, where we detail the error bars of all cosmological parameters.

Axion Early Dark Energy. For EDE we test the Axion Early Dark Energy (AEDE) model [43, 47–50] using **AxiCLASS**¹⁰ [51, 52] to compute the theory CMB power spectra in the likelihoods. In this model we sample over nine cosmological parameters: the six Λ CDM parameters, the initial value of the scalar field θ_i , the scale factor a_c at a critical time at which the scalar field starts to quickly decay, and the fractional energy of EDE at this time $f_{\text{ede}}(a_c)$. For this model the $R - 1$ threshold is increased to ~ 0.05 ¹¹ and we

¹⁰ <https://github.com/PoulinV/AxiCLASS>

¹¹ We increase the $R - 1$ threshold for this particular model because θ_i and $\log_{10}(a_c)$ are weakly constrained due to the fact that $f_{\text{ede}}(a_c)$ is compatible with zero. Hence the sampler will spend a lot of time trying to converge on these two parameters. We base our choice on previous analyses which also use this same value [43, 48].

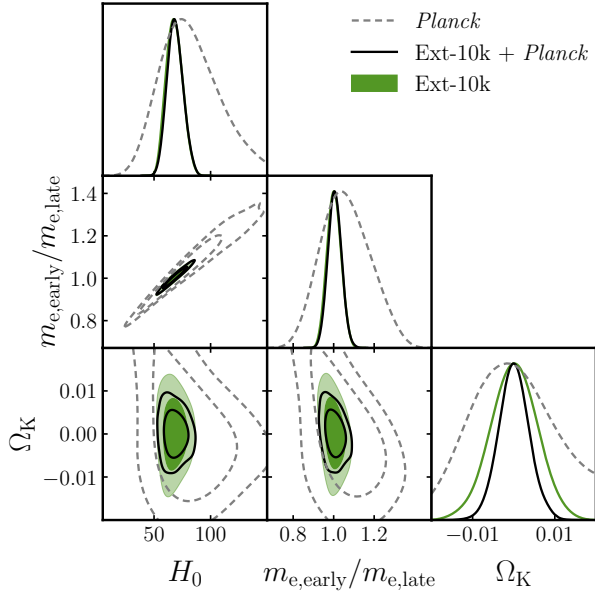


FIG. 9. SPT-3G Ext-10k TT/TE/EE/ $\phi\phi$ forecasts on the varying electron mass model in a curved universe. Contours correspond to the 68% and 95% confidence levels. In this plot, Ext-10k refers to Ext-10k TT/TE/EE/ $\phi\phi$ while *Planck* refers to our *Planck* mock likelihood.

also check that the chains have converged by splitting them into two random samples and ensuring they have, visually, the same posterior distribution. We show the results for SPT-3G Ext-10k TT/TE/EE/ $\phi\phi$ alone and combined with our *Planck* mock likelihood in Figure 10.

We forecast that the H_0 constraint from SPT-3G Ext-10k is 10% stronger than that from *Planck* alone and $f_{\text{ede}}(a_c)$ is 1.4 times better constrained with Ext-10k than with *Planck*. We also forecast that the constraints from SPT-3G Ext-10k in combination with *Planck* on H_0 and $f_{\text{ede}}(a_c)$ are a factor of 1.5 and 1.9 times tighter than *Planck* respectively. The cosmological parameter FoM of this model is computed for nine parameters. We find that Ext-10k TT/TE/EE/ $\phi\phi$ FoM is 73 times higher than that of *Planck*, and 321 times better when combining with *Planck*.

V. CONCLUSIONS

This work presents and validates the analysis choices for the Ext-10k survey of SPT-3G, a high-angular-resolution survey of $10\,000\,\text{deg}^2$ of the CMB from the South Pole. SPT-3G Ext-10k covers 25% of the total sky and is divided into 13 fields ranging from -20° to -80° in declination. These fields have different characteristics such as different atmospheric contamination, Galactic dust contamination, and noise properties, hence analyzing them independently is our strategy to take into account their particular features. In this paper, we ensure that choosing this analysis strategy

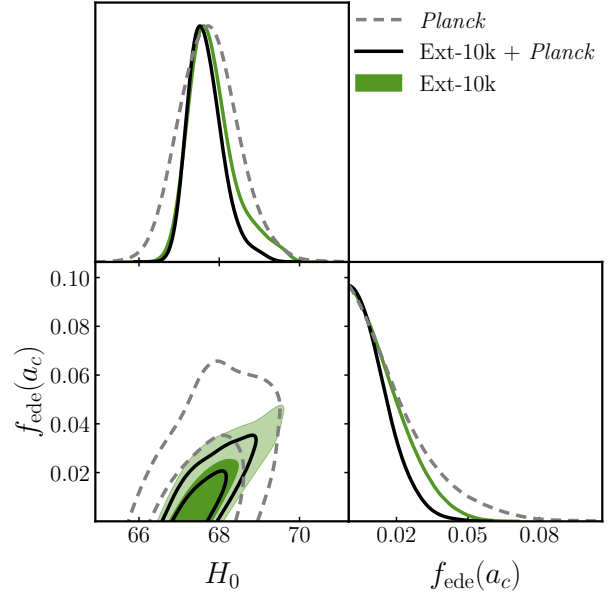


FIG. 10. SPT-3G Ext-10k TT/TE/EE/ $\phi\phi$ forecasts on the EDE model. Contours correspond to the 68% and 95% confidence levels. In this plot, Ext-10k refers to Ext-10k TT/TE/EE/ $\phi\phi$ while *Planck* refers to our *Planck* mock likelihood.

does not significantly impact the cosmological parameter constraints. We show that the loss of information from correlations between the fields and the slight decrease of f_{sky} due to the apodization of each individual patch contribute to an increase of less than 3% of the parameter error bars in ΛCDM .

We then extend the work of [11] by performing forecasts with a MCMC formalism with a more realistic patch-based analysis and foreground marginalization. We show that SPT-3G Ext-10k TT/TE/EE will constrain some ΛCDM parameters as strongly as *Planck*, and we confirm the results of [11] who showed that SPT-3G Ext-10k TT/TE/EE/ $\phi\phi$ constraints will be tighter than those of *Planck* for the ΛCDM cosmological parameters. We also expand the grid of extended models treated in [11] to include certain models with the potential to alleviate the Hubble tension, specifically models with varying electron mass and a model of EDE. We find that SPT-3G Ext-10k constraints on H_0 will be three times better than those of *Planck* in the varying electron mass case, both in a spatially flat or curved universe. We also forecast that SPT-3G Ext-10k will constrain H_0 10% stronger than *Planck* in the EDE model. These results show the promising potential of SPT-3G to detect or refute extended models designed to resolve the Hubble tension.

In this work, we do not use galaxy clusters or SZ power spectra, although SPT-3G data will provide additional cosmological constraints using these probes [53–55]. In this paper, we are interested in the improvement of constraints derived from CMB data only. In practice,

Parameter	m_e			$m_e + \Omega_K$			EDE		
	<i>Planck</i>	Ext-10k	Ext-10k+ <i>Planck</i>	<i>Planck</i>	Ext-10k	Ext-10k+ <i>Planck</i>	<i>Planck</i>	Ext-10k	Ext-10k+ <i>Planck</i>
$H_0 [\text{km s}^{-1} \text{ Mpc}^{-1}]$	$+20$ -30	$+7.3$ -8.5	$+6.4$ -7.4	$+20$ -30	$+6.7$ -7.9	$+6.6$ -7.5	$+0.67$ -0.77	$+0.37$ -0.68	$+0.33$ -0.50
$\Omega_b h^2$	0.0024	0.00090	0.00075	$+0.0025$ ± 0.0031	0.00083	0.00080	0.00019	0.000094	0.000085
$\Omega_c h^2$	0.013	0.0046	0.0038	$+0.014$ ± 0.016	0.0042	0.0039	$+0.0015$ ± 0.0019	$+0.00090$ ± 0.0014	$+0.00073$ ± 0.0010
$\log(10^{10} A_s)$	0.017	0.013	0.012	0.017	0.016	0.016	0.015	0.011	0.0098
n_s	0.0052	0.0039	0.0027	$+0.0057$ ± 0.0065	0.0059	0.0035	0.0054	0.0045	0.0032
σ_8	$+0.12$ -0.089	0.041	0.035	$+0.13$ -0.11	0.037	0.036	0.0087	$+0.0033$ -0.0037	0.0030
Ω_m	$+0.037$ -0.15	$+0.046$ -0.072	$+0.040$ -0.059	$+0.037$ -0.19	$+0.045$ -0.067	$+0.042$ -0.063	0.0087	0.0051	0.0042
$r_{\text{drag}} [\text{Mpc}]$	$+11$ -16	5.5	4.6	$+14$ -18	5.0	4.9	$+0.86$ -0.40	$+0.77$ -0.32	$+0.56$ -0.26
$m_{e,\text{early}}/m_{e,\text{late}}$	0.10	0.037	0.032	$+0.11$ -0.13	0.034	0.033	-	-	-
Ω_K	-	-	-	$+0.0090$ ± 0.011	0.0057	0.0038	-	-	-
$f_{\text{ede}}(a_c)$	-	-	-	-	-	-	< 0.0525	< 0.0364	< 0.0282
FoM/FoM _{<i>Planck</i>}	1	1.21×10^3	3.15×10^3	1	2.21×10^3	6.36×10^3	1	73.1	321

TABLE III. SPT-3G Ext-10k TT/TE/EE/ $\phi\phi$ forecasts of cosmological parameters in the varying electron mass and EDE models. Quoted values are error bars at the 68% confidence level or upper limits at the 95% confidence level. We do not show constraints on τ since they are prior driven. In this table, Ext-10k refers to Ext-10k TT/TE/EE/ $\phi\phi$ while *Planck* refers to our *Planck* mock likelihood. The last row presents the FoM relative to the one obtained with our *Planck* mock likelihood alone.

other data are used in combination with CMB to break degeneracies and further constrain extended models, such as BAO with SDSS [56–59] and DESI [6, 60], or type Ia Supernovae with Pantheon [61] and Pantheon+ [62]. In conjunction with these probes, SPT-3G Ext-10k will provide new insights into our understanding of the Universe.

VI. ACKNOWLEDGEMENTS

We thank Antony Lewis for scrutinizing the EDE results. The South Pole Telescope program is supported by the National Science Foundation (NSF) through awards OPP-1852617 and OPP-2332483. Partial support is also provided by the Kavli Institute of Cosmological Physics at the University of Chicago. Argonne National Laboratory’s work was supported by the U.S. Department of Energy, Office of High Energy Physics, under contract DE-AC02-06CH11357. The UC Davis group acknowledges support from Michael and Ester Vaida. Work at the Fermi National Accelerator Laboratory (Fermilab), a U.S. Department of Energy, Office of Science, Office of High Energy Physics HEP User Facility, is managed by Fermi Forward Discovery Group, LLC, acting under Contract No. 89243024CSC000002. The Melbourne authors acknowledge support from the Australian Research Council’s Discovery Project scheme (No. DP210102386). The Paris group has received funding from the European Research Council (ERC) under the European Union’s Horizon 2020 research and innovation

program (grant agreement No 101001897), and funding from the Centre National d’Etudes Spatiales. The SLAC group is supported in part by the Department of Energy at SLAC National Accelerator Laboratory, under contract DE-AC02-76SF00515. This work has made use of the Infinity Cluster hosted by Institut d’Astrophysique de Paris. We thank Stephane Rouberol for smoothly running this cluster for us. The CAPS authors are supported by the Center for AstroPhysical Surveys (CAPS) at the National Center for Supercomputing Applications (NCSA), University of Illinois Urbana-Champaign. This work relied on the NumPy library for numerical computations [63], the JAX library for automatic differentiation and GPU/TPU acceleration [20], and the Matplotlib library for plotting [64]. Posterior sampling analysis and plotting were performed using the GetDist package [36].

Appendix A: Polspice apodizesigma value determination for the *Wide* fields

1. The Polspice procedure

The temperature anisotropies map $\Theta(\hat{n})$ is defined from the temperature map $T(\hat{n})$ and the CMB mean temperature T as follows:

$$\Theta(\hat{n}) = \frac{T(\hat{n}) - T}{T}. \quad (\text{A1})$$

On the full sky, the temperature anisotropies decomposition into spherical harmonics is

$$\Theta(\hat{n}) = \sum_{\ell=0}^{+\infty} \sum_{m=-\ell}^{\ell} a_{\ell m}^T Y_{\ell m}(\hat{n}) \quad (\text{A2})$$

where the $a_{\ell m}^T$ coefficients can be written as:

$$a_{\ell m}^T = \int d\hat{n} \Theta(\hat{n}) Y_{\ell m}^*(\hat{n}). \quad (\text{A3})$$

An unbiased estimator of the CMB temperature power spectrum is then calculated from the $a_{\ell m}$ s as follows:

$$\hat{C}_{\ell}^{\text{TT}} = \frac{1}{2\ell + 1} \sum_{m=-\ell}^{\ell} a_{\ell m}^T a_{\ell m}^{T*}. \quad (\text{A4})$$

The ensemble average of \hat{C}_{ℓ} returns the theoretical spectrum $\langle \hat{C}_{\ell} \rangle = C_{\ell}^{th}$. However, when not observing the whole sky but only a portion of it we use a mask $W(\hat{n})$ which multiplies the temperature anisotropies map so that $\Theta(\hat{n})$ becomes $\Theta(\hat{n})W(\hat{n})$. The $a_{\ell m}$ s become $\tilde{a}_{\ell m}$ s and the associated temperature power spectrum is the pseudo power spectrum $\tilde{C}_{\ell}^{\text{TT}}$

$$\begin{aligned} \Theta(\hat{n}) &\longrightarrow \Theta(\hat{n})W(\hat{n}) \\ a_{\ell m}^T &\longrightarrow \tilde{a}_{\ell m}^T = \int d\hat{n} \Theta(\hat{n})W(\hat{n}) Y_{\ell m}^*(\hat{n}) \\ \hat{C}_{\ell}^{\text{TT}} &\longrightarrow \tilde{C}_{\ell}^{\text{TT}}. \end{aligned} \quad (\text{A5})$$

Equation 14 of [30] relates the pseudo power spectrum ensemble average to the theoretical CMB power spectrum as follows:

$$\langle \tilde{C}_{\ell} \rangle = \sum_{\ell'} M_{\ell\ell'} C_{\ell'}^{th} \quad (\text{A6})$$

where the matrix M describes the mode-mode coupling induced by the cut sky. Inverting this matrix would allow us to recover the theoretical power spectrum. In practice, we do not directly invert it because it is usually ill-conditioned, leading to an inaccurate inversion. In some cases the matrix may even be singular due to the fact that it is highly non-diagonal. In this case the inversion is impossible. For these reasons, a regularization is needed and Polspice's solution is to go to real space which is

the space of the correlation functions. In real space, Equation A6 is equivalent to the following product

$$\langle \tilde{\xi}(\theta) \rangle = w(\theta) \xi^{th}(\theta) \quad (\text{A7})$$

where $w(\theta)$ is the mask correlation function and θ is the angular separation in the sky. However a new problem arises when dividing by $w(\theta)$ since $w(\theta) = 0$ when θ is larger than the mask's physical dimensions. This would induce ringing in the multipole space. To solve this issue, Polspice introduces an apodization function $f^{\text{apo}}(\theta)$ which decays smoothly to zero such that

$$\hat{\xi}(\theta) = \begin{cases} \frac{f^{\text{apo}}(\theta)}{w(\theta)} \tilde{\xi}(\theta) & \theta < \theta_{\text{max}} \\ 0 & \theta > \theta_{\text{max}} \end{cases} \quad (\text{A8})$$

where θ_{max} is the `thetamax` parameter chosen by the Polspice user and cannot be higher than the masks' physical dimensions. Taking the ensemble average of the pseudo correlation function gives

$$\langle \hat{\xi}(\theta) \rangle = \begin{cases} f^{\text{apo}}(\theta) \xi^{th}(\theta) & \theta < \theta_{\text{max}} \\ 0 & \theta > \theta_{\text{max}} \end{cases}. \quad (\text{A9})$$

Going back to the multipole space, the last equation is equivalent to

$$\langle \hat{C}_{\ell} \rangle = \sum_{\ell'} K_{\ell\ell'} C_{\ell'}^{th} \quad (\text{A10})$$

where K is the Polspice kernel. For the full sky case the kernel is the identity matrix. Otherwise, it is necessary to account for this matrix in the window function during the analysis so that the data vector can be properly compared to the theory CMB power spectrum.

2. The apodizesigma parameter and the *Wide* fields case

We want to find the apodization function $f^{\text{apo}}(\theta)$ such that the kernel K is close to identity. In this work we choose $f^{\text{apo}}(\theta)$ to be a cosine function with `apodizetype` = 1 in Polspice:

$$f^{\text{apo}}(\theta) = \frac{1}{2} \left(1 + \cos \left(\frac{\pi \theta}{\sigma_{\text{apo}}^{PS}} \right) \right) \quad (\text{A11})$$

where σ_{apo}^{PS} is called the `apodizesigma` parameter and is chosen by the Polspice user. Larger values of this parameter include larger angular separations. We are interested in determining which values of `apodizesigma` σ_{apo}^{PS} and `thetamax` θ_{max} allow us to recover the less biased CMB power spectra. These parameters can vary from one field to another within the *Main*, *Summer*, and *Wide* fields. However, having the same parameters for all 13 fields of the Ext-10k survey implies having the same window function and this would simplify the analysis.

To estimate these two parameters we start from the *Planck* 2018 best-fit parameters [4] and we compute one power spectrum C_ℓ^{input} with CAMB. From this input spectrum we produce 1000 simulations of the CMB map in temperature and polarization with `healpy` [17, 65]. Then `Polspice` multiplies the simulated maps by the mask of the field we consider and computes the 1000 associated power spectra correcting them with `apodizesigma` and `thetamax`. A binning with bin size $\Delta\ell = 50$ is applied. Finally, we calculate the mean $\langle \hat{C}_\ell \rangle$ and the standard deviation σ_ℓ of these 1000 power spectra and we perform a χ^2 test where we compare the input spectrum with the mean spectrum as follows:

$$\chi^2 = \sum_\ell \left(\frac{\langle \hat{C}_\ell \rangle - \sum_{\ell'=0}^{6000} K_{\ell\ell'} C_{\ell'}^{\text{input}}}{\sigma_\ell / \sqrt{1000 - 1}} \right)^2. \quad (\text{A12})$$

The correlations between multipoles are neglected. The sum is done over an ℓ range of $100 \leq \ell \leq 4000$. We compute the reduced χ^2 from the number of degrees of freedom $N_{\text{dof}} = 78$ as $\chi_{\text{dof}}^2 = \frac{\chi^2}{N_{\text{dof}}}$.

We focus on the *Wide* fields for the rest of this appendix since a similar study has been previously done for the *Main* and *Summer* fields and showed that $\sigma_{\text{apo}}^{\text{PS}} = 30^\circ$ was an appropriate choice for those fields. We use the same apodized masks as the ones described in Section II. We set $\ell_{\text{max}} = 6000$ to produce the simulated maps from the input power spectrum. We set `tolerance` = 1.5×10^{-9} in `Polspice` which is the difference between two successive QQ and UU integrals in the convergence process to decorrelate E and B. We impose `thetamax` = `apodizesigma` and only vary the `apodizesigma` value. We tested $\sigma_{\text{apo}}^{\text{PS}} = 30^\circ$ and 45° for all nine fields because we know these values are reasonable for the *Main* and *Summer* fields. We also tested $\sigma_{\text{apo}}^{\text{PS}} = 10^\circ$ and 20° for the *Wide* a and b fields to see whether smaller values would improve the reduced χ^2 .

Table IV summarizes the χ_{dof}^2 values for the nine *Wide* fields. We only show results for $\sigma_{\text{apo}}^{\text{PS}} = 30^\circ$ and 45° since $\sigma_{\text{apo}}^{\text{PS}} = 10^\circ$ and 20° do not improve the reduced χ^2 in the *Wide* a and b cases. Moreover, $\sigma_{\text{apo}}^{\text{PS}} = 45^\circ$ cannot be applied for *Wide* e, g, h, and i because their physical dimensions are smaller than 45° . We conclude that $\sigma_{\text{apo}}^{\text{PS}} = 30^\circ$ is a reasonable choice for all the *Wide* fields if we want to use the same `Polspice` parameter for all the fields of the Ext-10k survey.

We apply the same methodology for the whole Ext-10k patch showed in Figure 1 which covers 23% of the total sky. We decide to test three different values of `apodizesigma`: 30° , 80° , and 120° . We find that $\sigma_{\text{apo}}^{\text{PS}} = 30^\circ$ and 80° give reasonable χ_{dof}^2 for TT, TE, and EE. We choose to use $\sigma_{\text{apo}}^{\text{PS}} = 80^\circ$ for the rest of the Ext10k_{joint} analysis because it allows us to include larger angular scales than 30° .

Wide	TT	EE	TE
a	1.06(1.16)	0.95(0.96)	0.99(1.27)
b	1.18(1.13)	0.94(0.99)	1.03(1.05)
c	1.35(1.37)	1.05(1.02)	1.27(1.26)
d	0.96(0.97)	1.14(1.19)	0.91(0.88)
e	0.99	1.20	1.38
f	0.80(0.87)	0.78(0.76)	0.86(0.82)
g	0.91	0.91	1.16
h	0.95	1.13	0.74
i	0.88	0.89	1.06

TABLE IV. χ_{dof}^2 values for $\sigma_{\text{apo}}^{\text{PS}} = 30^\circ$. Values in parentheses are for $\sigma_{\text{apo}}^{\text{PS}} = 45^\circ$. *Wide* e, g, h, and i only have values for 30° because their physical size is smaller than 45° and `apodizesigma` cannot have a larger value than the physical size.

Appendix B: Coadded covariance

In the Ext10k_{sep} case, we can calculate the total combined constraining power of the 13 separate fields assuming the coaddition of the separate power spectra after correction of field-specific nuisance and foregrounds parameters (see Appendix C4 of [18]). The coadded \hat{C}_ℓ covariance matrix can be calculated as:

$$\text{Cov}(\hat{C}_\ell^{\text{coadd}}, \hat{C}_\ell^{\text{coadd}}) = \sum_i w_i^2 \text{Cov}(\hat{C}_\ell^i, \hat{C}_\ell^i) \quad (\text{B1})$$

where $\hat{C}_\ell^{\text{coadd}}$ refers to the coaddition of the power spectra of the different fields:

$$\hat{C}_\ell^{\text{coadd}} = \sum_i w_i \hat{C}_\ell^i \quad (\text{B2})$$

and w_i is the weight associated to the i -th field calculated from its f_{sky} value (since we assume uniform noise levels across *Wide* fields)

$$w_i = \frac{f_{\text{sky}}^i}{\sum_j f_{\text{sky}}^j} \quad (\text{B3})$$

where w_i is the fraction of the total survey area covered by field i . This weighting scheme is due to the fact that the variance is proportional to $1/f_{\text{sky}}$ (see Equation 16 of [30]).

Appendix C: Transfer functions

Following [2] and Hivon et al., in prep, high-pass and low-pass filters are implemented to the real data in order to reduce large scale atmospheric contamination and

small scale aliasing¹², respectively. This can be described by a scalar transfer function $F(\ell)$ affecting the measured power spectra:

$$\langle C_\ell^F \rangle = F(\ell) \langle C_\ell^U \rangle \quad (C1)$$

in combination with a rescaling $H(\ell)$ of the covariance matrix diagonal:

$$\text{Cov}(C_\ell^F, C_\ell^F) = H(\ell) \text{Cov}(C_\ell^U, C_\ell^U) \quad (C2)$$

where C_ℓ^F and C_ℓ^U are the filtered and unfiltered power spectra, respectively. $F(\ell)$ is determined as the ratio of the power spectra of mock-observed maps to the power spectra of the underlying sky maps on the same apodized patch of sky. A set of slow but accurate simulations is used to calibrate the estimate of $F(\ell)$ based on faster but less accurate simulations run in large numbers to reduce the impact of cosmic variance. In this work we assume $H(\ell) = F(\ell)$ since this approximation is accurate at the 10% level for the *Main* and *Summer* fields Hivon et al., in prep. The covariances used in this work are therefore modified from their unfiltered values according to

$$\text{Cov}(C_\ell^F, C_\ell^F) = F(\ell) \text{Cov}(C_\ell^U, C_\ell^U) \quad (C3)$$

where the assumed $F(\ell)$ is shown in Figure 3. Hence, the relative covariance increases due to the data filtering as follows:

$$\frac{\text{Cov}(C_\ell^F, C_\ell^F)}{\langle C_\ell^F \rangle \langle C_\ell^F \rangle} = \frac{1}{F(\ell)} \frac{\text{Cov}(C_\ell^U, C_\ell^U)}{\langle C_\ell^U \rangle \langle C_\ell^U \rangle}. \quad (C4)$$

¹² Small scale aliasing refers to small scales being interpreted as larger scales in the reconstructed signal due to the grid resolution N_{side} which is too low for these multipoles.

[1] Ge, F., Millea, M., Camphuis, E., et al. Cosmology from CMB lensing and delensed EE power spectra using 2019–2020 SPT-3G polarization data. 2025, *Phys. Rev. D*, 111, 083534, doi: [10.1103/PhysRevD.111.083534](https://doi.org/10.1103/PhysRevD.111.083534)

[2] Camphuis, E., Quan, W., Balkenhol, L., et al. SPT-3G D1: CMB temperature and polarization power spectra and cosmology from 2019 and 2020 observations of the SPT-3G Main field. 2025, arXiv e-prints, arXiv:2506.20707, doi: [10.48550/arXiv.2506.20707](https://doi.org/10.48550/arXiv.2506.20707)

[3] Louis, T., La Posta, A., Atkins, Z., et al. The Atacama Cosmology Telescope: DR6 Power Spectra, Likelihoods and Λ CDM Parameters. 2025, arXiv e-prints, arXiv:2503.14452, doi: [10.48550/arXiv.2503.14452](https://doi.org/10.48550/arXiv.2503.14452)

[4] Planck Collaboration, Aghanim, N., Akrami, Y., et al. Planck 2018 results. VI. Cosmological parameters. 2020, *A&A*, 641, A6, doi: [10.1051/0004-6361/201833910](https://doi.org/10.1051/0004-6361/201833910)

[5] Breuval, L., Riess, A. G., Casertano, S., Yuan, W., Macri, L. M., Romaniello, M., Murakami, Y. S., Scolnic, D., Anand, G. S., & Soszyński, I. Small Magellanic Cloud Cepheids Observed with the Hubble Space Telescope Provide a New Anchor for the SH0ES Distance Ladder. 2024, *The Astrophysical Journal*, 973, 30, doi: [10.3847/1538-4357/ad630e](https://doi.org/10.3847/1538-4357/ad630e)

[6] DESI Collaboration, Abdul-Karim, M., Aguilar, J., et al. DESI DR2 Results II: Measurements of Baryon Acoustic Oscillations and Cosmological Constraints. 2025, arXiv e-prints, arXiv:2503.14738, doi: [10.48550/arXiv.2503.14738](https://doi.org/10.48550/arXiv.2503.14738)

[7] Ferreira, E. G. M., McDonough, E., Balkenhol, L., Kallosh, R., Knox, L., & Linde, A. The BAO-CMB Tension and Implications for Inflation. 2025, arXiv e-prints, arXiv:2507.12459, doi: [10.48550/arXiv.2507.12459](https://doi.org/10.48550/arXiv.2507.12459)

[8] Abitbol, M., Abril-Cabezas, I., Adachi, S., et al. The Simons Observatory: science goals and forecasts for the enhanced Large Aperture Telescope. 2025, *J. of Cosm. & Astropart. Phys.*, 2025, 034, doi: [10.1088/1475-7516/2025/08/034](https://doi.org/10.1088/1475-7516/2025/08/034)

[9] Benson, B. A., Ade, P. A. R., Ahmed, Z., et al. SPT-3G: A Next-Generation Cosmic Microwave Background Polarization Experiment on the South Pole Telescope. 2014, in *Proc. SPIE*, Vol. 9153, Millimeter, Submillimeter, and Far-Infrared Detectors and Instrumentation for Astronomy VII, 91531P, doi: [10.1117/12.2057305](https://doi.org/10.1117/12.2057305)

[10] Sobrin, J. A., Anderson, A. J., Bender, A. N., et al. The Design and Integrated Performance of SPT-3G. 2022, *Ap. J. Suppl.*, 258, 42, doi: [10.3847/1538-4365/ac374f](https://doi.org/10.3847/1538-4365/ac374f)

[11] Prabhu, K., Raghunathan, S., Millea, M., et al. Testing the Λ CDM Cosmological Model with Forthcoming Measurements of the Cosmic Microwave Background with SPT-3G. 2024, *Astrophys. J.*, 973, 4, doi: [10.3847/1538-4357/ad5ff1](https://doi.org/10.3847/1538-4357/ad5ff1)

[12] BICEP/Keck Collaboration, Ade, P. A. R., et al. The Latest Constraints on Inflationary B-modes from the BICEP/Keck Telescopes. 2022, arXiv e-prints, arXiv:2203.16556, doi: [10.48550/arXiv.2203.16556](https://doi.org/10.48550/arXiv.2203.16556)

[13] Khalife, A. R., Zanjani, M. B., Galli, S., Günther, S., Lesgourgues, J., & Benabed, K. Review of Hubble tension solutions with new SH0ES and SPT-3G data. 2024, *J. of Cosm. & Astropart. Phys.*, 2024, 059, doi: [10.1088/1475-7516/2024/04/059](https://doi.org/10.1088/1475-7516/2024/04/059)

[14] Carlstrom, J. E., Ade, P. A. R., Aird, K. A., et al. The 10 Meter South Pole Telescope. 2011, *PASP*, 123, 568, doi: [10.1086/659879](https://doi.org/10.1086/659879)

[15] Planck Collaboration, Akrami, Y., Ashdown, M., et al. Planck 2018 results. IV. Diffuse component separation. 2020, *A&A*, 641, A4, doi: [10.1051/0004-6361/201833881](https://doi.org/10.1051/0004-6361/201833881)

[16] Zebrowski, J. A., Reichardt, C. L., Anderson, A. J., et al. Constraints on Inflationary Gravitational Waves with Two Years of SPT-3G Data. 2025, arXiv e-prints, arXiv:2505.02827, doi: [10.48550/arXiv.2505.02827](https://doi.org/10.48550/arXiv.2505.02827)

[17] Górski, K. M., Hivon, E., Banday, A. J., Wandelt, B. D., Hansen, F. K., Reinecke, M., & Bartelmann, M. HEALPix: A Framework for High-Resolution Discretization and Fast Analysis of Data Distributed on the Sphere. 2005, *Astrophys. J.*, 622, 759, doi: [10.1086/427976](https://doi.org/10.1086/427976)

[18] Planck Collaboration, Aghanim, N., Arnaud, M., Ashdown, M., Aumont, J., Baccigalupi, C., Banday, A. J., Barreiro, R. B., Bartlett, J. G., Bartolo, N., & et al. Planck 2015 results. XI. CMB power spectra, likelihoods, and robustness of parameters. 2016, *A&A*, 594, A11, doi: [10.1051/0004-6361/201526926](https://doi.org/10.1051/0004-6361/201526926)

[19] Planck Collaboration, Ade, P. A. R., Aghanim, N., Arnaud, M., Ashdown, M., Aumont, J., Baccigalupi, C., Banday, A. J., Barreiro, R. B., Bartlett, J. G., Bartolo, N., & et al. Planck 2015 results. XIII. Cosmological parameters. 2016, *A&A*, 594, A13, doi: [10.1051/0004-6361/201525830](https://doi.org/10.1051/0004-6361/201525830)

[20] Bradbury, J., Frostig, R., Hawkins, P., Johnson, M. J., Leary, C., Maclaurin, D., Necula, G., Paszke, A., VanderPlas, J., Wanderman-Milne, S., & Zhang, Q. 2018, JAX: composable transformations of Python+NumPy programs, 0.3.13. <http://github.com/jax-ml/jax>

[21] Balkenhol, L., Tredafilova, C., Benabed, K., & Galli, S. candl: cosmic microwave background analysis with a differentiable likelihood. 2024, *A&A*, 686, A10, doi: [10.1051/0004-6361/202449432](https://doi.org/10.1051/0004-6361/202449432)

[22] Spurio Mancini, A., Piras, D., Alsing, J., Joachimi, B., & Hobson, M. P. COSMOPOWER: emulating cosmological power spectra for accelerated Bayesian inference from next-generation surveys. 2022, *MNRAS*, 511, 1771, doi: [10.1093/mnras/stac064](https://doi.org/10.1093/mnras/stac064)

[23] Piras, D., & Spurio Mancini, A. CosmoPower-JAX: high-dimensional Bayesian inference with differentiable cosmological emulators. 2023, *The Open Journal of Astrophysics*, 6, 20, doi: [10.21105/astro.2305.06347](https://doi.org/10.21105/astro.2305.06347)

[24] Balkenhol, L., Dutcher, D., Spurio Mancini, A., et al. Measurement of the CMB temperature power spectrum and constraints on cosmology from the SPT-3G 2018 T T , T E , and E E dataset. 2023, *Phys. Rev. D*, 108, 023510, doi: [10.1103/PhysRevD.108.023510](https://doi.org/10.1103/PhysRevD.108.023510)

[25] Lesgourgues, J. The Cosmic Linear Anisotropy Solving System (CLASS) I: Overview. 2011, arXiv e-prints, arXiv:1104.2932, doi: [10.48550/arXiv.1104.2932](https://doi.org/10.48550/arXiv.1104.2932)

[26] Lewis, A., & Challinor, A. 2011, CAMB: Code for Anisotropies in the Microwave Background, *Astrophysics Source Code Library*, record ascl:1102.026. <http://ascl.net/1102.026>

[27] Camphuis, E., Benabed, K., Galli, S., Hivon, E., & Lilley, M. Accurate cosmic microwave background covariance

matrices: Exact calculation and approximations. 2022, A&A, 668, A62, doi: [10.1051/0004-6361/202243948](https://doi.org/10.1051/0004-6361/202243948)

[28] Efstathiou, G. Myths and truths concerning estimation of power spectra: the case for a hybrid estimator. 2004, MNRAS, 349, 603, doi: [10.1111/j.1365-2966.2004.07530.x](https://doi.org/10.1111/j.1365-2966.2004.07530.x)

[29] García-García, C., Alonso, D., & Bellini, E. Disconnected pseudo- C_l covariances for projected large-scale structure data. 2019, J. of Cosm. & Astropart. Phys., 2019, 043, doi: [10.1088/1475-7516/2019/11/043](https://doi.org/10.1088/1475-7516/2019/11/043)

[30] Hivon, E., Górski, K. M., Netterfield, C. B., Crill, B. P., Prunet, S., & Hansen, F. MASTER of the Cosmic Microwave Background Anisotropy Power Spectrum: A Fast Method for Statistical Analysis of Large and Complex Cosmic Microwave Background Data Sets. 2002, Astrophys. J., 567, 2, doi: [10.1086/338126](https://doi.org/10.1086/338126)

[31] Chon, G., Challinor, A., Prunet, S., Hivon, E., & Szapudi, I. Fast estimation of polarization power spectra using correlation functions. 2004, MNRAS, 350, 914, doi: [10.1111/j.1365-2966.2004.07737.x](https://doi.org/10.1111/j.1365-2966.2004.07737.x)

[32] Omori, Y. Agora: Multi-Component Simulation for Cross-Survey Science. 2022, arXiv e-prints, arXiv:2212.07420, doi: [10.48550/arXiv.2212.07420](https://doi.org/10.48550/arXiv.2212.07420)

[33] Dutcher, D., Balkenhol, L., Ade, P. A. R., et al. Measurements of the E-mode polarization and temperature-E-mode correlation of the CMB from SPT-3G 2018 data. 2021, Phys. Rev. D, 104, 022003, doi: [10.1103/PhysRevD.104.022003](https://doi.org/10.1103/PhysRevD.104.022003)

[34] Manzotti, A., Hu, W., & Benoit-Lévy, A. Super-sample CMB lensing. 2014, Phys. Rev. D, 90, 023003, doi: [10.1103/PhysRevD.90.023003](https://doi.org/10.1103/PhysRevD.90.023003)

[35] Planck Collaboration, Aghanim, N., Akrami, Y., et al. Planck 2018 results. V. CMB power spectra and likelihoods. 2020, A&A, 641, A5, doi: [10.1051/0004-6361/201936386](https://doi.org/10.1051/0004-6361/201936386)

[36] Lewis, A. GetDist: a Python package for analysing Monte Carlo samples. 2019. <https://arxiv.org/abs/1910.13970>

[37] Torrado, J., & Lewis, A. Cobaya: code for Bayesian analysis of hierarchical physical models. 2021, J. of Cosm. & Astropart. Phys., 2021, 057, doi: [10.1088/1475-7516/2021/05/057](https://doi.org/10.1088/1475-7516/2021/05/057)

[38] Gelman, A., & Rubin, D. B. Inference from Iterative Simulation Using Multiple Sequences. 1992, Statistical Science, 7, 457. <http://www.jstor.org/stable/2246093>

[39] Uzan, J.-P. Varying Constants, Gravitation and Cosmology. 2011, Living Reviews in Relativity, 14, 2, doi: [10.12942/lrr-2011-2](https://doi.org/10.12942/lrr-2011-2)

[40] Sekiguchi, T., & Takahashi, T. Early recombination as a solution to the H_0 tension. 2021, Phys. Rev. D, 103, 083507, doi: [10.1103/PhysRevD.103.083507](https://doi.org/10.1103/PhysRevD.103.083507)

[41] Karwal, T., & Kamionkowski, M. Dark energy at early times, the Hubble parameter, and the string axiverse. 2016, Phys. Rev. D, 94, 103523, doi: [10.1103/PhysRevD.94.103523](https://doi.org/10.1103/PhysRevD.94.103523)

[42] Millea, M., & Seljak, U. Marginal unbiased score expansion and application to CMB lensing. 2022, Phys. Rev. D, 105, 103531, doi: [10.1103/PhysRevD.105.103531](https://doi.org/10.1103/PhysRevD.105.103531)

[43] Khalife, A. R., Balkenhol, L., Camphuis, E., et al. SPT-3G D1: Axion Early Dark Energy with CMB experiments and DESI. 2025, arXiv e-prints, arXiv:2507.23355, doi: [10.48550/arXiv.2507.23355](https://doi.org/10.48550/arXiv.2507.23355)

[44] Tredafilova, C., Khalife, A. R., & Galli, S. The end of easy phenomenology for CMB experiments: A case study in the dark sector. 2025, J. of Cosm. & Astropart. Phys., 2025, 094, doi: [10.1088/1475-7516/2025/05/094](https://doi.org/10.1088/1475-7516/2025/05/094)

[45] Takahashi, R., Sato, M., Nishimichi, T., Taruya, A., & Oguri, M. Revising the Halofit Model for the Nonlinear Matter Power Spectrum. 2012, Astrophys. J., 761, 152, doi: [10.1088/0004-637X/761/2/152](https://doi.org/10.1088/0004-637X/761/2/152)

[46] Mead, A. J., Peacock, J. A., Heymans, C., Joudaki, S., & Heavens, A. F. An accurate halo model for fitting non-linear cosmological power spectra and baryonic feedback models. 2015, MNRAS, 454, 1958, doi: [10.1093/mnras/stv2036](https://doi.org/10.1093/mnras/stv2036)

[47] Poulin, V., Smith, T. L., Karwal, T., & Kamionkowski, M. Early Dark Energy can Resolve the Hubble Tension. 2019, Physical Review Letters, 122, doi: [10.1103/physrevlett.122.221301](https://doi.org/10.1103/physrevlett.122.221301)

[48] Smith, T. L., Lucca, M., Poulin, V., Abellán, G. F., Balkenhol, L., Benabed, K., Galli, S., & Murgia, R. Hints of early dark energy in Planck, SPT, and ACT data: New physics or systematics? 2022, Phys. Rev. D, 106, 043526, doi: [10.1103/PhysRevD.106.043526](https://doi.org/10.1103/PhysRevD.106.043526)

[49] McDonough, E., & Scalisi, M. Towards Early Dark Energy in string theory. 2023, Journal of High Energy Physics, 2023, 118, doi: [10.1007/JHEP10\(2023\)118](https://doi.org/10.1007/JHEP10(2023)118)

[50] Cicoli, M., Licheri, M., Mahanta, R., McDonough, E., Pedro, F. G., & Scalisi, M. Early Dark Energy in Type IIB String Theory. 2023, Journal of High Energy Physics, 2023, 52, doi: [10.1007/JHEP06\(2023\)052](https://doi.org/10.1007/JHEP06(2023)052)

[51] Smith, T. L., Poulin, V., & Amin, M. A. Oscillating scalar fields and the Hubble tension: a resolution with novel signatures. 2020, Phys. Rev. D, 101, 063523, doi: [10.1103/PhysRevD.101.063523](https://doi.org/10.1103/PhysRevD.101.063523)

[52] Poulin, V., Smith, T. L., Grin, D., Karwal, T., & Kamionkowski, M. Cosmological implications of ultralight axionlike fields. 2018, Phys. Rev. D, 98, 083525, doi: [10.1103/PhysRevD.98.083525](https://doi.org/10.1103/PhysRevD.98.083525)

[53] Reichardt, C. L., Patil, S., Ade, P. A. R., et al. An Improved Measurement of the Secondary Cosmic Microwave Background Anisotropies from the SPT-SZ + SPTpol Surveys. 2021, Astrophys. J., 908, 199, doi: [10.3847/1538-4357/abd407](https://doi.org/10.3847/1538-4357/abd407)

[54] Raghunathan, S., Ade, P. A. R., Anderson, A. J., et al. First Constraints on the Epoch of Reionization Using the Non-Gaussianity of the Kinematic Sunyaev-Zel'dovich Effect from the South Pole Telescope and Herschel-SPIRE Observations. 2024, Phys. Rev. Lett., 133, 121004, doi: [10.1103/PhysRevLett.133.121004](https://doi.org/10.1103/PhysRevLett.133.121004)

[55] Bocquet, S., Grandis, S., Krause, E., et al. Multiprobe cosmology from the abundance of SPT clusters and DES galaxy clustering and weak lensing. 2025, Phys. Rev. D, 111, 063533, doi: [10.1103/PhysRevD.111.063533](https://doi.org/10.1103/PhysRevD.111.063533)

[56] Beutler, F., Blake, C., Colless, M., Jones, D. H., Staveley-Smith, L., Campbell, L., Parker, Q., Saunders, W., & Watson, F. The 6dF Galaxy Survey: baryon acoustic oscillations and the local Hubble constant. 2011, MNRAS, 416, 3017, doi: [10.1111/j.1365-2966.2011.19250.x](https://doi.org/10.1111/j.1365-2966.2011.19250.x)

[57] Ross, A. J., Samushia, L., Howlett, C., Percival, W. J., Burden, A., & Manera, M. The clustering of the SDSS DR7 main Galaxy sample - I. A 4 per cent distance measure at $z = 0.15$. 2015, MNRAS, 449, 835, doi: [10.1093/mnras/stv154](https://doi.org/10.1093/mnras/stv154)

[58] Alam, S., Ata, M., Bailey, S., et al. The clustering of galaxies in the completed SDSS-III Baryon Oscillation Spectroscopic Survey: cosmological analysis of the DR12 galaxy sample. 2017, *MNRAS*, 470, 2617, doi: [10.1093/mnras/stx721](https://doi.org/10.1093/mnras/stx721)

[59] Alam, S., Aubert, M., Avila, S., et al. Completed SDSS-IV extended Baryon Oscillation Spectroscopic Survey: Cosmological implications from two decades of spectroscopic surveys at the Apache Point Observatory. 2021, *Phys. Rev. D*, 103, 083533, doi: [10.1103/PhysRevD.103.083533](https://doi.org/10.1103/PhysRevD.103.083533)

[60] Adame, A. G., Aguilar, J., Ahlen, S., et al. DESI 2024 VI: cosmological constraints from the measurements of baryon acoustic oscillations. 2025, *J. of Cosm. & Astropart. Phys.*, 2025, 021, doi: [10.1088/1475-7516/2025/02/021](https://doi.org/10.1088/1475-7516/2025/02/021)

[61] Scolnic, D. M., Jones, D. O., Rest, A., et al. The Complete Light-curve Sample of Spectroscopically Confirmed SNe Ia from Pan-STARRS1 and Cosmological Constraints from the Combined Pantheon Sample. 2018, *Astrophys. J.*, 859, 101, doi: [10.3847/1538-4357/aab9bb](https://doi.org/10.3847/1538-4357/aab9bb)

[62] Brout, D., Scolnic, D., Popovic, B., et al. The Pantheon+ Analysis: Cosmological Constraints. 2022, *Astrophys. J.*, 938, 110, doi: [10.3847/1538-4357/ac8e04](https://doi.org/10.3847/1538-4357/ac8e04)

[63] van der Walt, S., Colbert, S. C., & Varoquaux, G. The NumPy Array: A Structure for Efficient Numerical Computation. 2011, *Computing in Science & Engineering*, 13, 22, doi: [10.1109/MCSE.2011.37](https://doi.org/10.1109/MCSE.2011.37)

[64] Hunter, J. D. Matplotlib: A 2D Graphics Environment. 2007, *Computing in Science and Engineering*, 9, 90, doi: [10.1109/MCSE.2007.55](https://doi.org/10.1109/MCSE.2007.55)

[65] Zonca, A., Singer, L., Lenz, D., Reinecke, M., Rosset, C., Hivon, E., & Gorski, K. healpy: equal area pixelization and spherical harmonics transforms for data on the sphere in Python. 2019, *Journal of Open Source Software*, 4, 1298, doi: [10.21105/joss.01298](https://doi.org/10.21105/joss.01298)